RESONANT VIBRATIONS OF MICROLITRE LIQUID DROPS

ROBERT TEMPERTON, BSc.

Thesis submitted to the University of Nottingham for the degree of Master of Science (by Research)

DECEMBER 2012

Abstract

The vibrational modes of water droplets supported on a surface (sessile drops) were excited by applying an impulse in the form of a short puff of nitrogen gas. An optical deflection technique was used to examine the modes of these oscillations in which laser light was scattered off the surface of the drops onto a photodiode. The time dependent intensity variations detected by the photodiode were Fourier transformed to give the vibrational spectra of the drops. The position and widths of the resonant peaks in these spectra were used along with a simple theory of droplet vibration to determine the surface tension and viscosity of the liquid. This theory models the resonant modes of the droplets as standing capillary wave states on the surface of a liquid bath of finite depth.

Surfaces patterned with parallel, periodic grooves were made using a variety of techniques. When a droplet of water was placed on one of these surfaces, the droplet was shown to wet anisotropically to the surface elongating the shape of the drop. The vibrational response of these aspherical droplets were measured as described above and the resulting vibrational spectra were shown to contain two closely spaced resonant peaks. These two peaks are shown to correspond to standing wave states forming along the profile lengths of the drop in the directions of the major and minor axes.

The vibrational response of droplets suspended from the end of a pipette tip (pendant drops) were also analysed using the same methods.

Contents

Chapter 1

Introduction

1.1 Motivation

The vibration of liquid droplets is a topic that has numerous potential applications in both science and technology. In particular, the vibration of droplets on surfaces (sessile drops) has been shown to aid processes such as drop atomisation. Here, liquid drops are placed on a surface that is vibrated in such a way as to excite the resonant modes of the droplet. If higher order modes are excited with large amplitudes, small secondary droplets are ejected from the surface of the sessile drop [1]. This has potential applications in technologies such as inkjet printing, spray coating and fuel injection [2] where the production of drops of a well defined size is required. Another example of the potential applications of the vibration of sessile droplets is that of the mixing of fluids where oscillating microlitre liquid droplets has been shown to accelerate the mixing process by about two orders of magnitude [3]. It has also been shown by authors such as Noblin et al.. [4], Mettu and Chaudhury [5], and Langley and Sharp [6] that the motion of droplets on surfaces can be controlled through vibration.

All of the above have many potential applications in the microfluidics industry which has been responsible for the development of mass produced products, such as the print heads used in ink-jet printers [7], through to emerging technologies such as the "lab-on-a-chip" concept [8]. Microfluidic "lab-on-a-chip" systems aim to revolutionise industries such as medical diagnostics where these devices have been proposed to be a potential solution to public heath issues in the developing world [9].

The vibration of droplets on surfaces also provides a technique that allows for the simultaneous measurement of surface tension and viscosity [10]. Surface tension can be measured by examining the dependence of resonant frequency on drop size [10, 11]. Viscosity of the liquids can be determined by considering the damping of the oscillations via measurements of the mechanical resonances [10, 12]. Although these measurements can be carried out on levitated droplets [13–16], developing the technique for sessile drops has many advantages as the experiments are quick and simple to carry out using relatively low cost equipment. The methods discussed in this thesis therefore have the potential to be developed into a tool of significant interest to physicists, chemists and materials scientists who have an interest determining key properties of small volumes of liquids.

There is also interest in how droplets behave when placed on patterned surfaces. It is well established that patterning [17, 18] and surface structure [19] can change the wetting properties of surfaces. We have already mentioned that the vibration can be used to drive the motion of drops across a surface. Langley and Sharp showed that the direction of this motion can be controlled by using patterning to create a gradient in the wetting properties. Spatial variations in contact angles on these surfaces were shown to give rise to a net force which acts on the drop. However, this force is only generated around the three phase contact line (the perimeter of the drop that is in contact with both the solid surface and the surrounding air) and is often not sufficiently large

enough to overcome frictional interactions between the drop and the surface. Vibrating the drop near its resonant frequency allows the drop to overcome these iterations and to sample the energy configurations of the surrounding areas of the surface. This results in the motion of the drop down the energy gradient defined by the structured surface [6]. The same concept can be applied to induce ratchet-like motion of droplets. [20, 21].

In this thesis we exploit the anisotropic wetting properties of patterned surfaces to elongate the shape of sessile droplets [17]. We go onto study the vibrational response of such droplets and compare the results to that of conventional drops that are shaped like spherical caps.

1.2   Background

The study of droplet oscillations dates back to the 19th century when Lord Rayleigh developed a theory which described the oscillation of capillary waves around an inviscid (zero viscosity) liquid sphere [22]. Lamb went on to consider the oscillations of a viscous sphere [23] which was shortly followed by Thomson's (Lord Kelvin's) study of the gravitational oscillations of rotating water in 1880 [24]. In 1958, Chandrasekhar extended all of these ideas in his investigation of oscillations on a viscous liquid globe [25]. Since then, numerous experiments have been carried out where these ideas have been applied to levitated droplets of both metals [14, 26–29] and non metals [13, 30–32]. Many techniques have been used to levitate droplets including acoustic [31, 33–36], aerodynamic [15, 37, 38], electrostatic [16, 28, 39] and magnetic [13, 14, 30, 32, 40–43] levitation methods. Firstly, acoustic levitation allows droplets to be suspended from the nodes of high pressure standing waves [34] [33]. Authors such as Trinh and Wang have used acoustic levitation to study the resonant frequencies, the damping of oscillations, and other phenomena, such as drop fission, that occur when levitated droplets are driven at small [36] and large [35] amplitudes. Shen

et al. examined the shape oscillations of acoustically levitated water drops [31] and showed their resonant behaviour matched those predicted by Rayleigh [22]. Other techniques include aerodynamic levitation, where a flow of gas through a nozzle is used to to suspend a droplet [38], and electrostatic levitation, where a charged droplet can be suspended in an electric field. Droplets vibrated under these conditions have been used to measure properties of liquids such as surface tension [15, 16] and viscosity [16, 28].

Another popular technique used is that of magnetic levitation. This technique has also been used by authors to levitate magnetic materials allowing non-contact measurements of their surface tension and viscosity [14, 27] by measuring the oscillations of the suspended droplets. The technique of magnetic levitation is more broadly used (i.e. without utilising oscillations) to make measurements of the density by measuring the equilibrium shape of levitated drops of a known mass. From the equilibrium shape the volume can be inferred allowing the density to be calculated [14]. It is also possible to levitate diamagnetic materials, such as water, in a sufficiently large magnetic field (16-17T [13]) [13, 30, 42, 44]. This has created interest in the biological community allowing, for example, the effect of weightlessness on the growth of bacteria [45] and motion of small animals, such as the fruitfly [43], to be studied with ease. This technique has also been used by Hill and Eaves who utilised the work of the early pioneers of droplet oscillation, such as Rayleigh and Lamb, to study the oscillations of water droplets allowing the measurement of surface tension and viscosity of water [13]. Further studies by Hill and Eaves have investigated the effect of electric charge on the oscillations [32].

Recently there has also been a large interest in the vibration of sessile droplets. Numerous authors have derived theories that attempt to describe the behaviour of the vibration of sessile drops. These include the work of Strani and Sabetta [46, 47], Celestini and Kofman [48], and Lyubimov et al. [49]. However, the most intuitive of the models in the literature comes from Noblin

et al. [50] who utilise the simple idea of standing waves forming around the sur-
face of the droplets. Noblin's work has also been used by other authors such as
Sharp et al. who demonstrated the potential of using sessile drop vibration as
a tool for determining the properties of liquids. In the same way that has been
discussed for levitated drops, the resonant properties of sessile drops were used
in order to measure the surface tension and viscosity of water [10]. Sharp then
goes on to develop an understanding of how the oscillations in sessile drops are
damped by the bulk interactions between molecules, frictional interactions at
the drop/substrate boundary and by contamination of the drop's surface [12].

It is the simple ideas of Noblin and Sharp that underpin the work of this thesis.
The techniques described by Sharp [10, 12] are used to extend Noblin's model
of droplet vibration [50] to include oscillations of elongated/aspherical sessile
drops. These same techniques were used to examine whether Noblin's model
can also be applied to describe the oscillations of pendant drops (droplets
suspended off the end of a needle, pipette tip or similar).

Chapter 2

Theory

2.1 Surface tension and the capillary length

This study focuses on investigating the vibrational behaviour of droplets that are dominated by surface tension. Surface tension, γ, describes the ability of a liquid to resist its surface being deformed. It can be defined by considering the amount of work, δW, that needs to be done on a liquid in order to increase its surface area by an amount δA such that

$$\delta W = \gamma \delta A \tag{2.1}$$

This expression correctly implies that surface tension has units of Nm^{-1} or Jm^{-2}. Both units are equivalent but the latter is usually reserved for discussions of surface or interfacial energies (which are more general terms that apply to solid and gas interfaces as well as liquids).

In order to consider the origin of this effect, the simplest situation to picture is
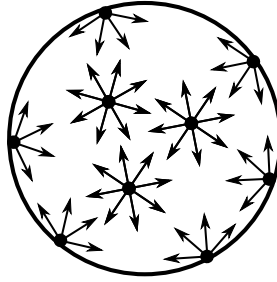
Figure 2.1: *A diagram of a sphere of liquid, in the bulk of which, intermolecular interactions act equally in all directions. At the surface, the interactions are unbalanced. Surface tension originates from the energy penalty associated with these unbalanced interactions.*

that of a sphere suspended in free space. Here, the drop is in static equilibrium and is dominated by surface tension. As pictured in Figure 2.1, in the bulk of the liquid, there is no net force on the molecules as these intermolecular interactions act equally in all directions. At the surface this is not the case and the unbalanced interactions between the surface and bulk molecules have an energy penalty associated with them. This is the origin of surface tension which, if no net external forces act on a droplet, forces the liquid into spheres as this shape has the smallest possible surface area for its volume [51].

Above a critical length-scale called the capillary length, the effect of gravity on large isolated droplets becomes significant. As the drops deform under the influence of gravity, a change in surface area occurs and surface tension acts as a restoring force. Below this critical length, surface tension (or capillary) effects dominate. The capillary length, l_c, therefore defines the regime where surface tension and gravity have an equal influence. An approximate value for the capillary length can be found by considering the pressures acting on the droplet as a result of surface tension and gravity [52]. Firstly, the pressure on a droplet due to surface tension originates from the pressure difference between the inside and outside of a drop. As discussed above, surface tension causes curvature in the liquid/air interface which results in a pressure difference across the interface. This pressure difference can be defined from the Young-Laplace equation [53] which, for a spherical body, gives the pressure difference between

the inside and outside of the drop to be

$$\Delta P = 2\frac{\gamma}{R} \qquad (2.2)$$

where ΔP is called the Laplace pressure and R is the radius of the drop [54]. Secondly, the pressure exerted on a liquid due to the force of gravity is called the hydrostatic pressure. For a liquid of density ρ, the hydrostatic pressure at a depth a in the liquid is given by

$$p = \rho g a \qquad (2.3)$$

where $g = 9.81\text{ms}^{-2}$ is the acceleration due to gravity [55]. We can approximate the value of the capillary length at equilibrium by setting $\Delta P = p$ and by letting $a = R = l_c$ (i.e. setting the characteristic size of the drop to equal the capillary length). Equating equations 2.3 and 2.2 in this way gives

$$l_c \sim \sqrt{\frac{\gamma}{\rho g}} \qquad (2.4)$$

For clean water at room temperature and pressure (with a surface tension $\gamma = 72.8\text{Nm}^{-1}$ [56] and of density $\rho = 998\text{kgm}^{-3}$ [57]) in air, equation 2.4 gives the capillary length to be $l_c = 2.7\text{mm}$. In comparison, methanol has a lower surface tension of $\gamma = 23.0\text{Nm}^{-1}$ [58] and a density of $\rho = 790\text{kgm}^{-2}$ [59]. Equation 2.4 therefore gives the capillary length of methanol to be $l_c = 1.7\text{mm}$.

2.2 Levitated drops

2.2.1 Capillary waves on the surface of levitated droplets

This study focuses on analysing the resonant properties of liquid droplets. The easiest situation to consider is that of a spherical drop suspended in free space. This can be achieved using, for example, the diamagnetic forces that arise from placing materials such as water in a strong magnetic field in order to counter the force of gravity. This allows droplets, even those with dimensions larger than the capillary length, to form near perfect spheres.

When such a drop is perturbed, capillary waves travel around the surface of the droplet. The resonant modes of these oscillations were first described by Lord Rayleigh who said that for a spherical drops with radius R, the angular frequencies at which resonance occurs are given by

$$\omega = \left(\frac{l(l-1)(l+2)\gamma}{\rho R^3} \right)^{1/2} \tag{2.5}$$

where l is the mode number and γ and ρ are the surface tension and density of the liquid respectively [22]. The frequencies are therefore given by $f = \frac{\omega}{2\pi}$.

In the case of diamagnetically levitated drops, the situation is not as simple as the idealistic scenario presented by Rayleigh as the diamagnetic forces, which are proportional to $B\nabla B$ (where B is the field strength of the applied magnetic field), exert an additional restoring force on the surface of the drop [13].

2.2.2   Damping

The viscous damping of the capillary waves described by Rayleigh has been studied by both Lamb [23] and later Chandrasekhar [25] who both show that waves with amplitude A, decay exponentially with respect to time so that $A \sim e^{-\Gamma t}$. The decay constant, Γ, is shown to have a linear relationship with viscosity, η, as described by

$$\Gamma = \frac{\eta(l-1)(2l+1)}{\rho R^2} \tag{2.6}$$

where as before R is the radius and l is the mode number.

2.3   Sessile drops

2.3.1   The shape of sessile drops

A sessile drop is a drop that is supported on a substrate. When a liquid drop is placed onto a solid surface in a gaseous environment, the drop forms a shape that is determined by the balance of the surface energies associated with solid/liquid, solid/gas and liquid/gas interfaces (γ_{SL}, γ_{SG} and γ_{LG} respectively). The surface energy of the liquid-gas interface is equivalent to the surface tension, γ, of the liquid as discussed in Section 2.1.

In order for a drop to be stationary, the forces acting on its three-phase contact line (the perimeter of the liquid in contact with both the solid surface and the gaseous environment) must be in equilibrium. This balance can be described in terms of γ_{SL}, γ_{SG} and γ_{LG} as shown in Figure 2.2. The mathematical description of this equilibrium state comes from resolving the three
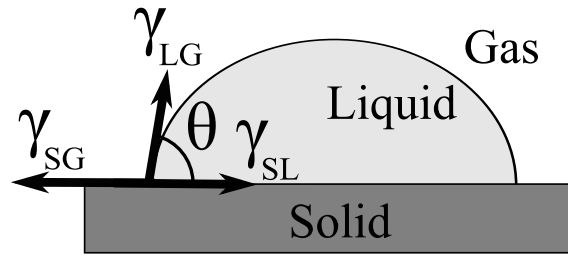
Figure 2.2: *The balance of surface energies around the three-phase contact line of a sessile droplet in equilibrium. γ_{SG},γ_{SL} and γ_{LG} are surface energies of the solid-gas, solid-liquid and liquid-gas interfaces. θ is the contact angle the drop forms with the surface.*

forces acting per unit length (surface tensions) at the 3-phase contact line as given by Young's equation

$$\gamma_{SG} = \gamma_{SL} + \gamma_{LG} \cos \theta \tag{2.7}$$

where θ is the angle formed between the drop edge and the substrate. θ is called the equilibrium contact angle and is a measure of how well the liquid wets the surface [60]. Shallow contact angles are observed when the liquid wets well to the surface and, for the case of water, large contact angles occur on "superhydrophobic" surfaces. On these surfaces, the interface between the liquid and solid is so unfavourable that the water beads up into shapes that are a close approximation to spheres. The variation in contact angle for different surfaces is shown in Figure 2.3. Here, the same volume of water, 5μL, was placed on Silicon, Gold, PDMS and a superhydrophic surface (made by annealing a glass slide in a candle flame as outlined in Appendix B) which show water contact angles of 20°, 90°, 110° and 150° respectively.

Assuming the substrate is perfectly clean and flat, the balance of surface energies should be the same at every point around the three-phase contact line giving a constant contact angle. However, in reality, getting a perfectly clean and flat surface is nearly impossible and often results in an effect called contact an-
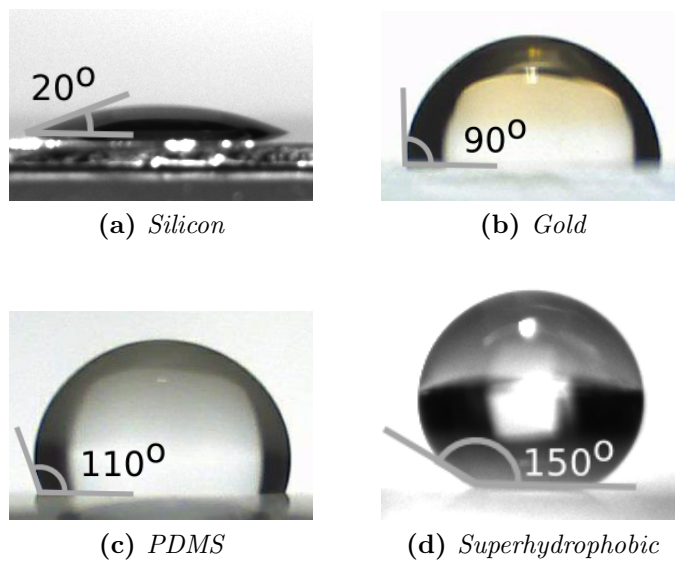
(a) *Silicon*   (b) *Gold*

(c) *PDMS*   (d) *Superhydrophobic*

Figure 2.3: *Photographs showing the contact angles of* $5\,\mu L$ *water droplets placed on (a) silicon, (b) gold, (c) polydimethylsiloxane (PDMS) and (d) a superhydrophobic surface (made using the technique outlined in Appendix B).*

gle hysteresis. This occurs due to local variations in surface roughness and/or chemical contamination meaning the interfacial energies vary from point to point on the surface. This results in the contact angle varying between a minimum and maximum value called the receding angle, θ_R, and advancing angle, θ_A respectively [61]. It has been shown by Tadmor [62] that the equilibrium contact angle, i.e. the angle given in Young's equation, is

$$\theta = \arccos\left(\frac{r_A \cos\theta_A + r_R \cos\theta_R}{r_A + r_R}\right) \tag{2.8}$$

where r_A and r_R are given by

$$r_i = \left(\frac{\sin^3\theta_i}{2 - 3\cos\theta_i + \cos^3\theta_i}\right)^{1/3} \tag{2.9}$$

where $i = A$ or R.

For sessile droplets with a radius of curvature less than the capillary length of

(a) $10\mu L$ (b) $50\mu L$ (c) $100\mu L$
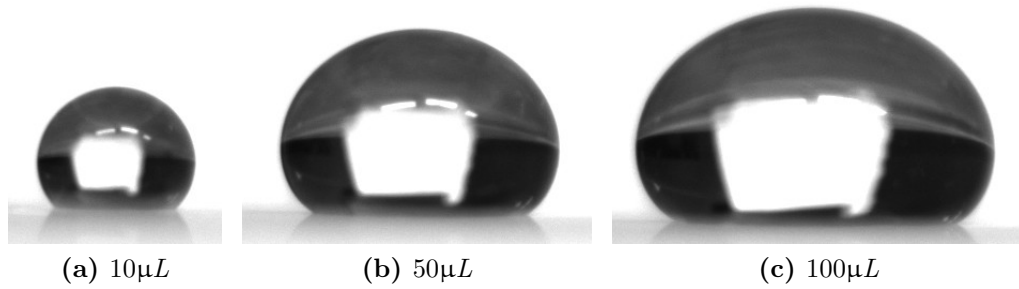
Figure 2.4: *Photographs showing the puddling of droplets as the size of the drop exceeds the length-scale defined by the capillary length. Here **(a)** shows a drop with dimensions smaller than this length-scale forming a spherical cap and **(b)** and **(c)** above this length-scale where gravity is flattening the drop.*

the liquid used, the drops appear to take the shape of a spherical cap. If the size of the droplet is increased so that the radius of curvature is greater than the capillary length, gravity starts to dominate over surface tension causing the spherical cap to flatten into a puddle. This is shown in Figure 2.4 where 10µL, 50µL and 100µL of water were placed on a hydrophobic substrate.

2.3.2   Profile length

Another important variable in determining the vibrational behaviour of small sessile liquid drops is the profile length of the drop, L. If we look at the droplet from the side, the profile length is the arc length that the liquid/air boundary forms. The plane passing through the center of a spherical cap is drawn out in Figure 2.5 where the profile length, L, is annotated. A consideration of the geometry of a circle allows us to relate the profile length to the contact angle and radius of curvature, R, of the spherical cap such that $L = 2R\theta$.

Many of the approaches taken in this study utilise this length rather than the contact angle (as is used by Sharp [10] [12]) as it's arguably more intuitive when considering surface oscillations of droplet although, it is stressed here that the use of the profile length and the contact angle in formulating the expressions for the vibrational frequencies of small sessile drops give equivalent expressions.
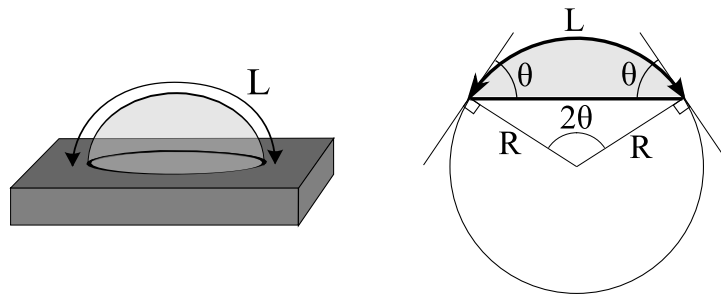
Figure 2.5: *Diagram showing the drop profile of a spherical cap. The profile length, L, radius of curvature, R, and the contact angle θ are defined as shown.*

2.3.3 Capillary-gravity waves on sessile droplets

When capillary waves are excited on the surface of sessile drops, the physics is slightly different to that described in Section 2.2 where spherical, levitated droplets are discussed. The fact that the droplet's contact line is pinned to the solid substrate means that all points around this line must act as vibrational nodes. We can treat the resonant modes on the surface of the drop as standing waves which satisfy the condition that

$$L = \frac{n\lambda}{2} \tag{2.10}$$

where n and λ are the mode number and wavelength of the standing wave states. Diagrams showing the first three allowed modes of these oscillations, n=2, 3 and 4, are included in Figure 2.6. n=1 oscillations would require either the contact line to slip across the surface or for the volume of the liquid to change. As the liquid is incompressible and the contact line remained pinned to the surface in all experiments, n=1 oscillations are not permitted. n=2 oscillations therefore represent the fundamental mode.

This simple approach of describing the oscillations as standing wave states around the droplet profile was proposed by Noblin et al. [50]. These authors showed that the surface waves on sessile drops can be modelled as capillary
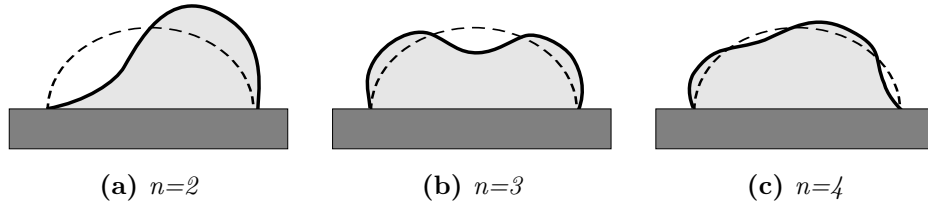
(a) *n=2*   **(b)** *n=3*   **(c)** *n=4*

Figure 2.6: *Diagrams showing the first 3 allowed modes of oscillation (n=2,3,4). The n=1 mode is not allowed as the contact line of the drop is pinned to the surface and the liquid is incompressible - both of these conditions can not remain true for n=1 oscillations.*

waves on a bath of liquid of length, L. The dispersion relation for capillary-gravity waves on the surface of a liquid bath of depth d is

$$\omega^2 = \left(gq + \frac{\gamma}{\rho}q^3 \right) \tanh(qd) \tag{2.11}$$

where ω is the angular frequency and q, the wavenumber, is defined as $q = \frac{2\pi}{\lambda}$. ρ and γ are the density and surface tension of the liquid respectively and the tanh term compensates for the bath being of a finite, rather than infinite, depth [63].

If the effects of gravity are ignored, which is a valid assumption for drops with a radius of curvature less than the capillary length, this expression can be simplified as the gq term becomes small in comparison to the $\frac{\gamma}{\rho}q^3$ term. Since $q = \frac{2\pi}{\lambda}$ and $\omega = 2\pi f$, substitution of Equation 2.10 into Equation 2.11, gives an expression for the frequency of oscillations in terms of the droplet's profile length:

$$f^2 = \frac{n^3\pi\gamma}{4\rho L^3}\alpha^2 \tag{2.12}$$

where, for convenience, we have defined a constant α such that $\alpha^2 = \tanh(qd) = \tanh\left(\frac{n\pi d}{L}\right)$.

As per the Noblin model, the depth of the bath can be approximated to the average height of the drop, $\bar{h}$ [50] giving $\alpha^2 = \tanh(q\bar{h})$. Noblin approximates this average height to be the ratio of drop's volume and basal area. Sharp's approach in compensating for the bath not being of infinite depth was to determine a scaling factor between the frequencies experimentally observed and those predicted by the dispersion relation for an infinitely deep bath. The scaling factor, observed across the entire range of contact angles investigated by Sharp and his co-authors, corresponds to $\alpha \approx 0.81$ [10].

2.3.4   Damping of capillary-gravity waves on sessile drops

The origins of damping in sessile drops is a more complex problem than that of levitated drops as the interactions between the drop and the substrate create additional damping mechanisms. Damping of capillary waves on sessile droplets has been recently considered Sharp [12]. Again, we assume the oscillations decay exponentially with time such that the amplitude scales with $e^{-\Gamma t}$ where Γ is the damping coefficient. Firstly, and most prominently, Sharp considers bulk viscous damping which has a damping coefficient of given by

$$\Gamma_{bulk} = \frac{2\eta}{\rho}q^2 \tag{2.13}$$

where η is the viscosity of the fluid [64]. From the definition of the wavenumber, $q = {2\pi}/{\lambda}$, and the knowledge that a half integer number of wavelengths fit around the droplet profile (Equation 2.10) we get

$$\Gamma_{bulk} = \frac{2\eta}{\rho}\left(\frac{n\pi}{L}\right)^2 \tag{2.14}$$

Since, for a spherical cap $L = 2R\theta$, this has the same ${\eta}/{R^2}$ dependence as the

levitated case (equation 2.6).

Damping can also result from the interaction of the drop with the substrate. This so-called boundary layer damping originates from the condition that the drop is pinned to the substrate. The three phase contact line is therefore stationary and can not slip across the surface of the substrate. As described by Milner [65] and Sharp [12], for surface waves on a bath of liquid, in order for the liquid at the edge of the bath to be stationary, the velocity of the liquid falls to zero from the value in the bulk over a distance given by

$$\delta = \left(\frac{\eta}{\pi \rho f} \right)^{1/2} \tag{2.15}$$

with damping coefficient

$$\Gamma_{boundary} = \frac{\omega \delta}{L_{bath}} \tag{2.16}$$

where ω is the angular frequency of the oscillations and L_{bath} is the length of the liquid bath. Assuming that the surface of the droplets behaves like such a bath of liquid such that $L_{bath} = L$ where L is the profile length of the drops, we can use our expression for the frequency (equation 2.12) to get

$$\Gamma_{boundary} = \left(\frac{n^3 \pi^2 \alpha^2 \eta \gamma}{\rho L^5} \right)^{1/2} \tag{2.17}$$

Sharp shows that for liquids with a range of viscosities, the L^{-2} dependence on Γ predicted by bulk viscous damping (equation 2.14) closely matches the measurements taken for droplets with contact angles larger than $\sim 70°$. For droplets with shallower contact angles, boundary layer damping should be taken into account. However, for the purposes of this study, the contact an-

gles are not in the regime where boundary layer damping effects need to be considered.

2.3.5 Aspherical sessile droplets

The above model of surface oscillations in droplets was designed to consider spherical drops with a single radius of curvature, profile length and contact angle. This study aims to investigate the vibrational response of drops that do not have this geometrical simplicity.

Aspherical drops can be made by patterning a surface with a series of periodic grooves running in one direction [17] (see Figure 2.7). Introducing grooves that typically have periodicity and amplitudes of the order of microns, increases the contour length in one direction relative to the other. As described previously, the shape of a drop is determined by the balance of interfacial energies around the 3-phase contact line. When a drop is placed on such a patterned surface, it naturally deforms reducing the basal area in the direction perpendicular to the grooves in order to maintain this equilibrium. These aspherical drops can be modelled as ellipsoidal caps from which we can define a long and short profile length as shown in Figure 2.7.

Cummings and Blackburn considered the effect of having a levitated drop that was asymmetric in it's three axes [66]. This work has since been used by authors such as Vicente et.al [29] and Hill et al. [67] where the concept has been applied to compensate for the slightly aspherical drop shapes that result from asymmetries in the potential of the magnetic traps used to levitate droplets. Cummings showed that for each mode of oscillation, you expect three peaks in the vibrational spectra corresponding to vibrations along the three axis of the drop.
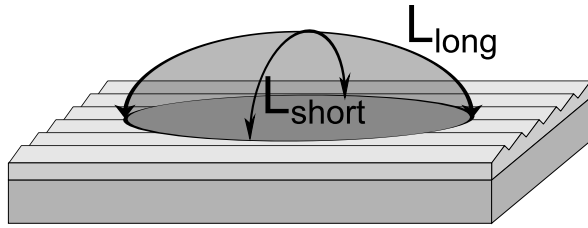
Figure 2.7: *Diagram showing an aspherical drop formed by placing a liquid into a corrugated surface. The two profile lengths, L_{long} and L_{short}, are defined as the arc length in the major and minor axis of the drop.*

In extension to Cummings' work, we present the hypothesis that, for a sessile drop that is elongated in a single direction, there will be a splitting of each vibrational mode into two (rather than three) closely spaced modes. In the spherical case, standing waves form along the droplet profile. For the elongated/aspherical case, we have a major and minor axis with a long and a short profile length (see Figure 2.7). We would therefore expect two peaks in the frequency spectra of such a drop with the lower and higher frequency peaks corresponding to oscillations along the long and short profile lengths (major and minor axes) respectively. The third vibrational peak predicted by Cummings' work, in the case of sessile drops, would require the contact line to slip across the surface. Considering the pinning of the contact line and the frictional interactions between the fluid near the contact line and the substrate, this slipping is not permitted suppressing the third mode.

2.4 Pendant drops

A pendant drop is a drop that is suspended on the end on a needle or similar tube. For a pendant drop with a diameter smaller than the capillary length, l_c, the effects of gravity are negligible and a pendant drop is essentially an upside down sessile drop. In this regime, surface tension dominates and forces the liquid to take the form of a spherical cap. As the diameter approaches the capillary length, gravity starts to distort the shape of the drop. At a
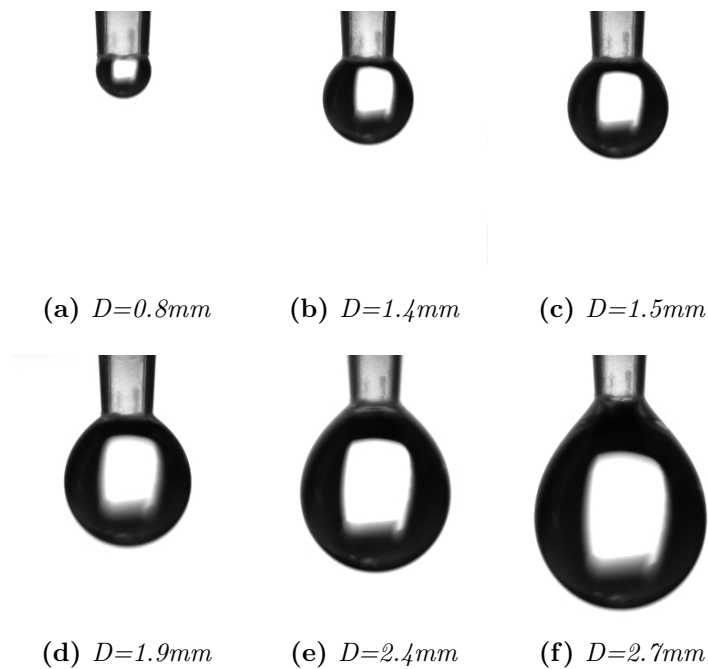
(a) *D=0.8mm* **(b)** *D=1.4mm* **(c)** *D=1.5mm*

(d) *D=1.9mm* **(e)** *D=2.4mm* **(f)** *D=2.7mm*

Figure 2.8: *Droplets of water (that had a surface tension of $\gamma \approx 60mNm^{-1}$- see Section 6) suspended on the end of a pipette tip. As the diameter begins to exceed the capillary length $L_c \sim 2.5mm$ (calculated using equation 2.4), the drops become elongated due to gravity.*

critical size, the weight of the droplet dominates and surface tension is no longer enough to hold the drop on the end of the tip.

Photographs of various sizes of pendant drops are shown in Figure 2.8. Drops with radius of curvature much less than the capillary length have a spherical shape. As the drop diameter approaches the capillary length of the liquid, $l_c \sim 2.5mm$ in this case, the shape of the drops start to deform as a result of their weight.

Considering that the physics of small pendant drops is essentially the same as that of sessile drops, we predict the vibrational response of such drops to behave in the same way. This study therefore aims to apply Noblin's model for oscillations of sessile drops on surfaces [50], as disussed in Section 2.3.3, to the pendant case.

Chapter 3

Experimental Methods

3.1 Vibration of sessile drops

Oscillations in sessile droplets can be excited in a number of ways. Commonly, the oscillations are driven, for example by attaching the substrate, on which a drop sits, to a loudspeaker [50] or piezoelectric actuator [2]. Here, the resonant modes are determined by performing a frequency sweep and monitoring the change in shape of the drop. These methods have been adapted by authors such as Mettu and Chaudhury [68] who have driven the oscillations using white noise. This technique drives the droplets at all frequencies simultaneously and with the same amplitude. It is also possible to excite resonance by perturbing the drop with a short impulse that provides broadband excitation. All oscillations apart from those that meet the criteria for resonance will decay away instantaneously leaving the drop ringing at its resonant frequencies. This technique has been utilised previously by Sharp et al. where a short puff of air was used to perturb the droplet [10] [12]. It is this concept that is used extensively throughout this study.

Originally, the impulse took the form of a puff of air that was produced by
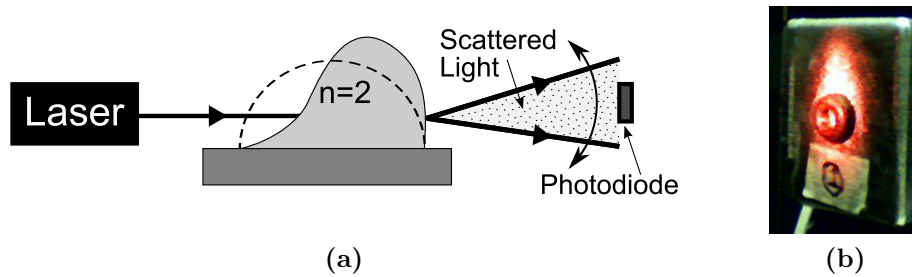
(a)   **(b)**

Figure 3.1: *(a) Diagram showing how the vibrational response of sessile droplets is measured. Laser light is scattered off the surface of the drop onto a photodiode. Oscillations of the drop (such as the n=2 mode shown) were excited using a small puff of nitrogen gas. The resulting motion of the scattered light was detected using the photodiode. (b) shows scattered light falling onto the photodiode (which is in the center of the black ring in the middle of the photograph).*

gently blowing on the droplets. In order to provide a greater degree of control over the impulse, a system was devised whereby a puff of nitrogen gas was used to apply the impulse to the drops. A solenoid valve (SMC Pneumatics), controlled using Matlab (Mathworks) and a National Instruments data acquisition card (USB-6008), allowed precise control of the duration of the impulse. Pneumatic regulators provided control of the gas pressure and thus the intensity of the impulse. The nozzle was also mounted in a fixed position relative to the droplets. These three control measures allowed a significantly greater degree of repeatability of the impulse whilst reducing the likelihood of the impulse causing additional contamination of the droplet.

Attempts were also made to apply the impulse mechanically by placing the substrate onto a piezoelectric transducer. Rapidly charging/discharging the piezo resulted in a very sudden but small vertical displacement which provided a small perturbation that could excite resonance in low viscosity liquids. Even for low viscosity fluids such as water, the amplitude of the measured oscillations was very low resulting in a low signal to noise ratio. The approach of using a puff of nitrogen to perturb the drops was therefore preferable.

The oscillations were measured using a simple laser light scattering technique. Light from a Helium Neon (HeNe 633nm) laser was scattered off the surface of

the droplets (see Figure 3.1a). The cross section of the scattered light consisted of a diffuse scattering pattern which oscillated as the droplet was vibrated. Placing a photodiode (RS Components, BPX65) in the cone of scattered laser light, allowed time dependent variations in intensity to be measured. A photodiode was used as the detector because it had a non-uniform response over its active area thus enhancing any changes due to varying intensity gradients in the system. This maximised the voltage fluctuations measured across the photodiode. The photodiode was connected to a home built amplifier circuit from which the time dependent signal was acquired using the data acquisition card. Fourier transformation of this data produced a power spectrum giving the vibrational response of the droplets. From these spectra, the positions and widths of the resonant frequency peaks could be extracted where the width (full width at half maximum), Δf, is equivalent to the damping coefficients discussed in Sections 2.2.2 and 2.3.4 [12]. An example of the acquired time dependent data and resulting vibrational spectra are included in Figure 3.2.

The apparatus described above was mounted on an optical rail. As the experiments progressed, we gradually developed the set-up to allow the alignment of the components to be controlled with higher precision and greater ease. The final set-up is shown in Figure 3.3. The laser was mounted using two lens mounts on optical posts. The sample stage included high precision x, y and z control (through translation stages) and a 360° rotation stage. The photodiode, built on the side of the box containing the amplification circuit, could also be translated in 3 axes.

Photographs were taken of the droplets in order to measure their profile lengths. Originally a simple 1-megapixel webcam (Philips SPC100NC) was used with the camera software packaged with Microsoft Windows XP. Later a Manta-G125B (Allied Vision Technologies) camera was used with either the "GigE veiwer" or "AVT UniCam" software (Allied Vision Technologies). The photographs taken using both cameras gave comparable results once processed.
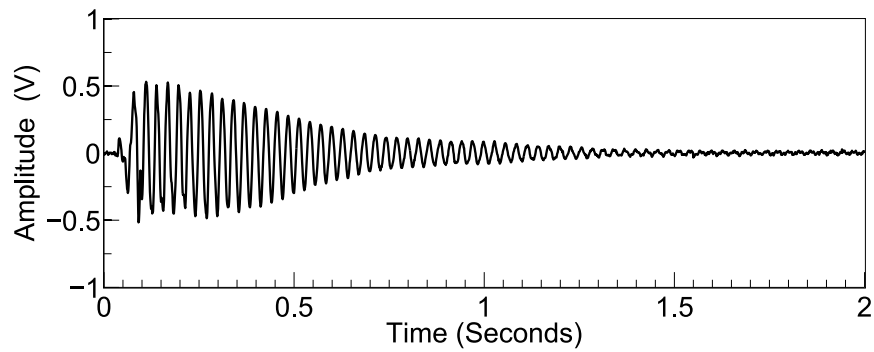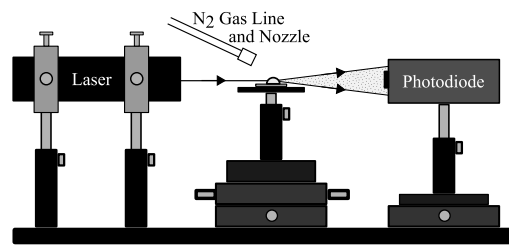
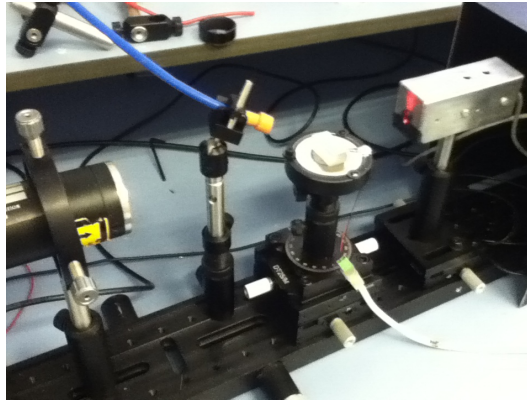(a) *Time dependant photodiode signal*
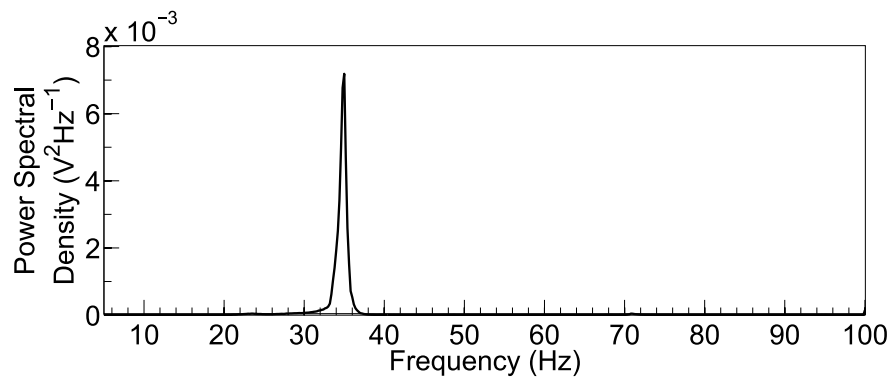
(b) *Vibrational Spectra*

Figure 3.2: *(a) Time dependent photodiode signal collected for a spherical* $10\mu L$ *water droplet on a PDMS (polydimethylsiloxane) substrate. (b) The Fourier transformation of the time dependent signal, shown in (a), shows the resonant peak of the fundamental n=2 mode.*

(a) *Schematic*

(b) *Photograph*

Figure 3.3: *The apparatus used for investigating vibrations in sessile drops. From left to right in both figures we have the laser, the nitrogen gas line, a drop on the sample stage and the photodiode. The piezo used is also visible in the photograph.*

However, the lens on the webcam produced photographs with a noticeable fish-eye effect if the drop was not positioned in the center of the field of view. This was not an issue with the Manta camera as more appropriate lenses could be selected. The manta camera also allowed for a much finer control over the focus resulting in slightly sharper images.

The photographs were analysed using a program we wrote using Matlab in order to extract the profile of the droplet. An example of a photograph and the extracted profile is shown in Figure 3.4. The profiles were calibrated using photographs of a steel rule with 0.5mm divisions allowing the profile lengths of the drops to be calculated. The plots of the droplet profiles were also used to calculate the average height of aspherical drops where ellipses were fitted to these profiles (see Appendix A.2).
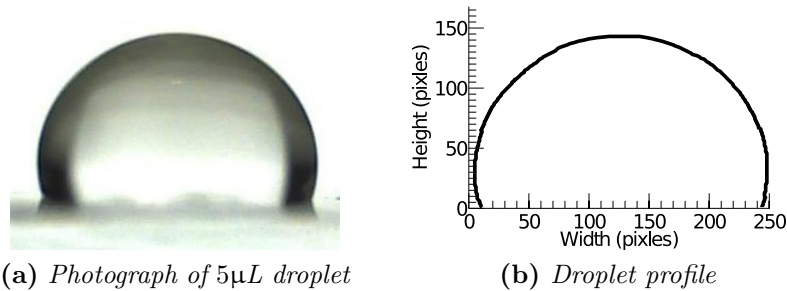
(a) *Photograph of* 5µL *droplet*   **(b)** *Droplet profile*

Figure 3.4: *An example photograph of a* 5µL *droplet of water on a PDMS (Poly-dimethylsiloxane) substrate and the line profile extract from the photograph using Matlab.*

3.2 Vibration of pendant drops

The approach taken to excite and measure the vibrational response of pendant drops was the same as described previously for the sessile drop experiment. A puff of nitrogen gas provided the perturbation and the vibrational spectra were obtained using the same laser light scattering technique. Photographs of droplets were taken using the Manta-G125B camera and processed using the same Matlab program in order to extract the profile lengths. The images were calibrated using the widths of the pipette tips (visible in all the photographs) which were originally measured using an Olympus BX51M optical microscope.

Drops were suspended from the end of disposable micro-pipette tips (Scientific Laboratory Supplies, PIP9044) attached to 0.5mL polypropylene syringes (Becton Dickinson). The syringes were supplied with bevel point needles attached which were removed in order to attach the pipette tips. The pipette tips and syringes were carefully cleaned by ultrasonicating them in both a surfactant and solvents such as isopropanol and methanol. Extensively cleaning the rubber plungers stopped them moving through the syringe smoothly so these were very quickly rinsed in methanol. This thorough cleaning process was carried out in order to minimise contamination of the liquids used in the experiments as this was shown to be an issue affecting the repeatability of the data collected.
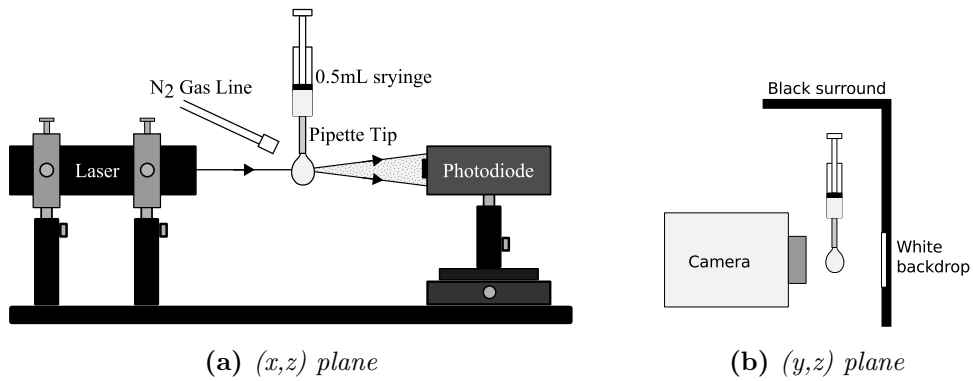
(a) *(x,z) plane*   **(b)** *(y,z) plane*

Figure 3.5: *Diagram showing the apparatus used to determine vibrational spectra for pendant drops shown in the planes parallel, figure **(a)**, and perpendicular, figure **(b)**, to the laser beam.*

3.3   Vibration of magnetically levitated drops

A vertical-bore superconducting solenoid magnet (Cryogenic Ltd.), with field strengths of $\sim 17T$, was used to diamagnetically levitate water based droplets. The principle of the experimental setup was similar to that of the sessile and pendant droplet experiment but, as shown in Figure 3.6, optical fibres were used to take light to and from the bore of the magnet. Light from a simple laser diode (HeNe 633nm) was focussed onto the end of a cut fibre using a single lens. The other end of this fibre was held a few centimetres below the droplet using a custom made enclosure that fitted inside the bore. The droplet acted like a lens focussing the light onto a second fibre suspended above the drop. The other end of this fibre was coupled to a photodiode inside a shielded metal box.

The concept of the optical system slightly differs from the sessile drop case. Fluctuations in the shape of the drop that result from the shape oscillations caused small time dependent oscillations in the position of the focal point. As the fibre was held in a fixed position near the focal point of the steady state drop, low amplitude shape oscillations result in relativity dramatic fluctuations in the measured light intensity. The fibre was not placed exactly on the focal point in order to reduce the sensitivity of the system to small center

Optical fibre
to photodiode

Air nozzle

Optical fibre
from laser-diode

(a) *Diagram of the apparatus inside the bore of the magnet*

(b) *The magnet*

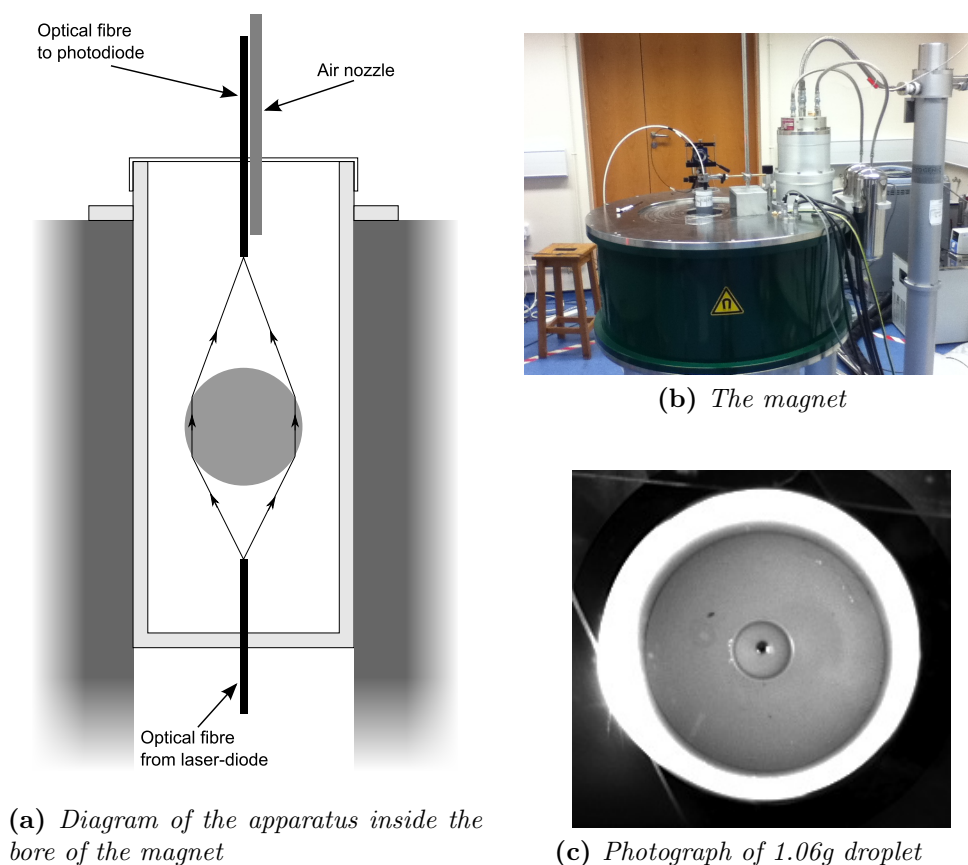**(c)** *Photograph of 1.06g droplet*

Figure 3.6: *(a) Schematic of the set-up used to measure the vibrational spectra of droplets suspended in a magnetic trap inside the bore of the superconducting magnet pictured in (b). (b) Photograph taken from above a 1.06g water droplet. The black spot in the middle of the droplet is an image of the optical fibre below.*

of mass oscillations (motion of the drop in the magnetic trap). The custom built enclosure completely surrounded the apparatus in the bore which helped minimise these oscillations by reducing air movement.

Drops were placed into the magnetic trap using a standard disposable glass pipette. The mass of the pipette was measured using a digital balance before and after the liquid was injected into the trap giving the mass of the drop. After the drop was placed in the levitation point, it was common to have to wait ~30 minutes for the center of mass oscillations to decay to a small enough amplitude to carry out the experiments.

As with the sessile drops, capillary waves on the surface of the the levitated drops were excited by applying an impulse. One end of a flexible plastic tube was held directly above the drop and a pipette bulb was attached to the other end. By swinging the tube and hitting the bulb onto a hard surface, a very short puff of air travelled down the tube and perturbed the droplet. The signal from the photodiode was fed into a data acquisition card card (National Instruments PCI-6225) and was processed in Matlab. Again, following the method used for the sessile drop experiments (see Section 3.1), this time dependent signal was Fourier transformed to extract the vibrational spectra of the droplets.

For each drop, at least 3 spectra were collected. After applying each impulse, it took ~15 minutes for the center of mass oscillations to decay to a sufficiently low amplitude to take the next repeat measurement. The size of the center of mass oscillations was monitored using the test panel in National Instruments "Measurement and Automation Explorer" software. Once all the required data was collected, the drop was drawn out of the magnet using a paper towel. Weighing the paper towel before and after withdrawing the drop gave the final mass of the drop telling us how much mass had been lost through evaporation whilst taking the measurements. Typically, the mass loss over an

entire experiment was $\sim 2\%$ which had a negligible impact on the position of the frequency peaks.

The radius of the droplet, R, was inferred from the mass, m, of the drop. Assuming a spherical shape, this gives

$$R = \left(\frac{3m}{4\pi\rho}\right)^{1/3} \tag{3.1}$$

3.4   Surfaces with anisotropic wetting properties

As described in Section 2.3.5, sessile droplets can be elongated by patterning a surface with grooves that run in one direction. A variety of methods were used to fabricate grooved surfaces and these are outlined below.

3.4.1   Wrinkled metal films

Wrinkled aluminium or gold substrates were made using the technique illustrated in Figure 3.7. PDMS (polydimethylsiloxane) was moulded into rectangular substrates using custom made PTFE (polytetrafluoroethylene) moulds. Two types of PDMS were used: The first type, Sylgard "184 Silicone Elastomer", was mixed with it's cross linking agent in a 10:1 ratio, de-gassed in a vacuum chamber and cured at 150° for 30 minutes. The second type, "Silicone Rubber Compound" (RS Components) was supplied in a single tube and, after being poured into the mould, was left to set under ambient conditions over a period of 24 hours. In this second case, a thin membrane of cured PDMS very quickly appeared meaning it could not be degassed without large

bubbles forming under the surface of the substrate. Before it set, any bubbles had to be quickly popped using a needle. The RS Components PDMS made a more flexible and less brittle substrate but was a less clean system than the Sylgard elastomer. Despite its potential contamination issues, the RS components PDMS was the preferred elastomer for making substrates that were put under strain.

Once cured, the PDMS was peeled out of the mould and cut to size using a scalpel before being placed in a home-built stretching device. As pictured in Figure 3.7, this consisted of a sample holder that could be detached from a micrometer-controlled vice. The sample holder gripped the PDMS substrates on two opposite sides which were then pulled apart using the vice. This applied a strain to the PDMS which was maintained when the sample holder was detached from the vice. The sample holder and strained PDMS were then placed in a thermal evaporator where a thin film of aluminium or gold of thickness 50-250nm was deposited onto the surface of the PDMS. A quartz crystal thin film monitor was used to measure the thickness of the metal film. At this stage, the metal film was not under any stress, but once taken out of the evaporator, the strain in the PDMS was released which caused the metal film to compress. This resulted in the formation of periodic wrinkles in the metal film that run in the direction perpendicular to the applied strain.

The act of relaxing the strain also caused cracking of the film in the direction parallel to the applied strain. This is because, as the applied strain is released, there is a slight expansion in the elastomer in the direction perpendicular to the applied strain. Releasing the large strains applied to the PDMS ($\sim 50\%$) result in a stress in the direction parallel to wrinkles that is greater than the yield strength of the metal. Above this critical point, the film will no longer deform elastically causing fractures in the film.

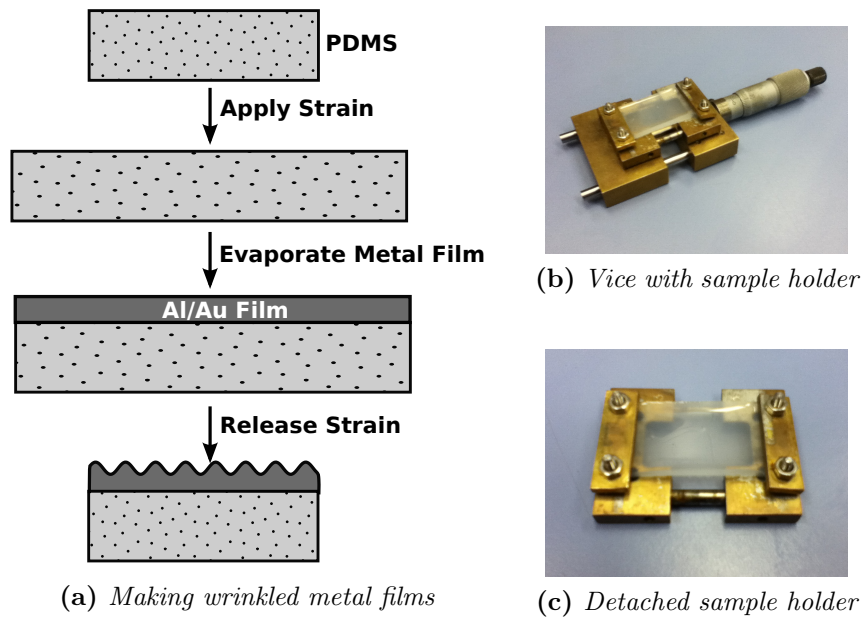The periodicity and amplitude of the wrinkles formed could be selected by

(a) *Making wrinkled metal films*

(b) *Vice with sample holder*

(c) *Detached sample holder*

Figure 3.7: *(a) shows the method used to wrinkle metal films. PDMS was moulded into sheets with a thickness of $\sim 2mm$. A home built device, pictured in (b), was used to apply a strain of 50 % to the PDMS. The top part of this device could be locked off and detached as shown in (c) and was then placed in a thermal evaporator where$\sim 100nm$ of aluminium or gold was deposited . When the strain was released, wrinkles with height and periodicity $\sim$microns were formed.*

controlling the strain applied to the elastomer and/or the thickness of the metal film. Although these dependencies were not studied here, they have been investigated by Langley and Sharp [6] who compared experiment with theory showing that increasing the thickness of the film causes a linear increase in both the periodicity and amplitude of the wrinkles. Langley also showed that increasing the strain applied to the elastomer decreases the periodicity and increases the amplitude of the wrinkles formed.

Figure 3.8 shows optical micrograph images and an AFM (atomic force microscope) line profile of the surface of an example substrate made using this technique. This substrate was made by evaporating 150nm of aluminium onto PDMS with a 40% strain applied. Releasing this strain caused wrinkles to form with a period of ~ 15 microns and a peak to peak amplitude of ~ 5 microns. The cracks shown in the micrographs propagate all the way through the metal film exposing droplets placed on the surface to the underlying elastomer.
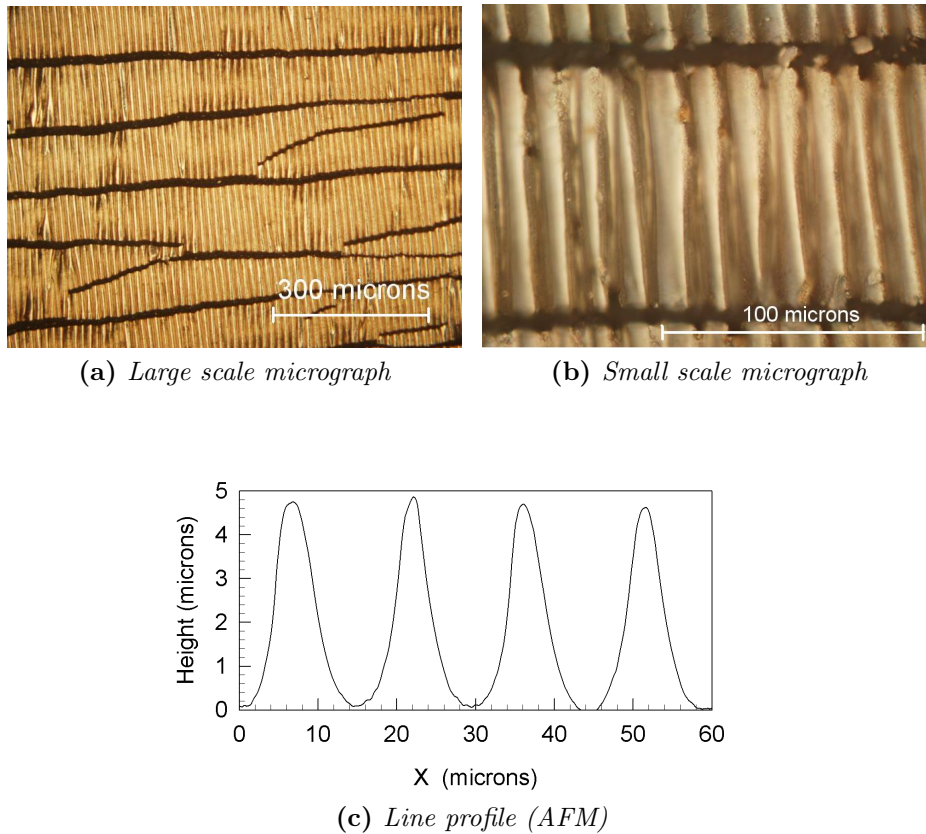
(a) *Large scale micrograph*

(b) *Small scale micrograph*

(c) *Line profile (AFM)*

Figure 3.8: *(a) and (b) show two micrograph images of the same wrinkled aluminium substrate that was made by evaporating a 150nm thick film of aluminium onto a PDMS substrate with a 40% strain applied. (a) shows the large scale features of the substrate including the wrinkling and cracks in the aluminium film. (b) shows the wrinkles of period $\sim$ 15 microns in more detail. (c) shows a height profile of the wrinkles obtained using atomic force microscopy (AFM) showing the wrinkles have a height of $\sim$ 5 microns.*
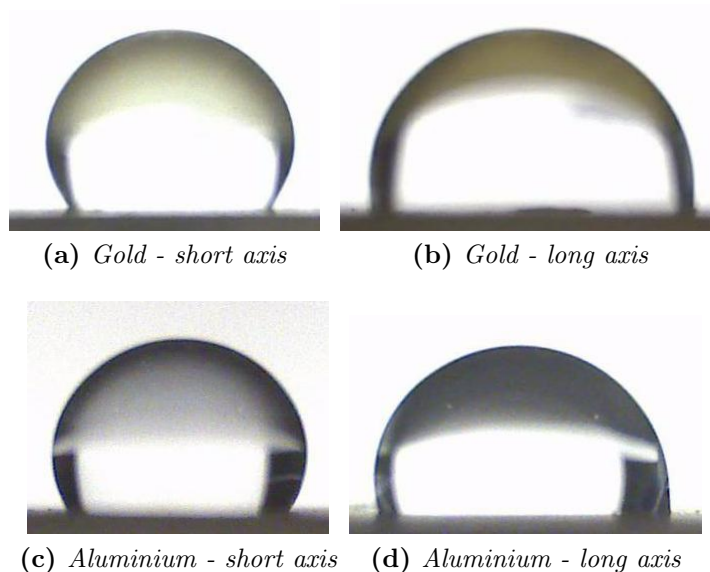
(a) *Gold - short axis*   **(b)** *Gold - long axis*

(c) *Aluminium - short axis*   **(d)** *Aluminium - long axis*

Figure 3.9: *Photographs showing the short and long droplet profiles for* $10\mu L$ *droplets of water placed on wrinkled gold and aluminium surfaces. Both substrates were made by thermally evaporating 100nm of the metal onto PDMS that has a strain of 50% applied.*

This was a potential source of contamination as contaminants, such as excess monomer or cross linking agent from the elastomer, could be transported into the droplet. It also adds a further complication in understanding the shape the droplets that form as interfaces between water droplets and the elastomer have a different surface energy to that of the water/metal interface resulting in a potential increase in contact angle hysteresis.

When water droplets were placed on wrinkled aluminium surfaces, markings showing the basal area of the drop were visible when the drop was removed. The exact origin of these was never confirmed. It was originally thought to be a result of oxidation of the aluminium but similar markings, although to a much lesser extent, were visible on wrinkled gold films which should not oxidise. However, when a drop was placed on a plane gold surface (gold thermally evaporated onto a glass microscope slide), the markings were not apparent. This implies that whatever caused the markings was coming from the regions of the PDMS substrate that were exposed to the water droplets by the cracks in the metal films.

Example photographs of the two drop profiles formed when 10µL of water was placed on gold and aluminium wrinkled surfaces are included in Figure 3.9. Both of these substrates were made by evaporating 100nm of the metal onto PDMS (RS Components) substrates with a strain of 50% applied.

3.4.2 Wrinkled polymer films

Two methods of producing wrinkled polymer films were attempted which are outlined in Figure 3.10. The first method involved producing a wrinkled aluminium film using the method outlined in Section 3.4.1 and using it as a mould. De-gassed Sylgard PDMS was poured over the metal surface and annealed in an oven at $150^{o}C$. The two layers could then be pulled apart. Residue aluminium was removed from the surface by dissolving it in a weak sodium hydroxide solution. The surface was then cleaned using de-ionised water and methanol (which did not noticeably swell the PDMS).

The second method aimed to apply the same principle used to produce wrinkled metal substrates. A 2% solution of polystyrene (PS) in toluene was spin cast onto a glass microscope slide at 3000rpm and was floated on the surface of a bath of water. A PDMS substrate held under strain by the sample holder was submerged in the bath of water and raised so that the PS film was placed on the substrate. Whilst still under strain, the PDMS/PS system was heated at 100°C to drive off any water and anneal the PS to the PDMS. Once cooled, the strain was removed and the PS film showed comparable wrinkling behaviour to that observed in metal films as described in Section 3.4.1.

Optical micrographs of images showing the results of both of these techniques are shown in Figure 3.11.

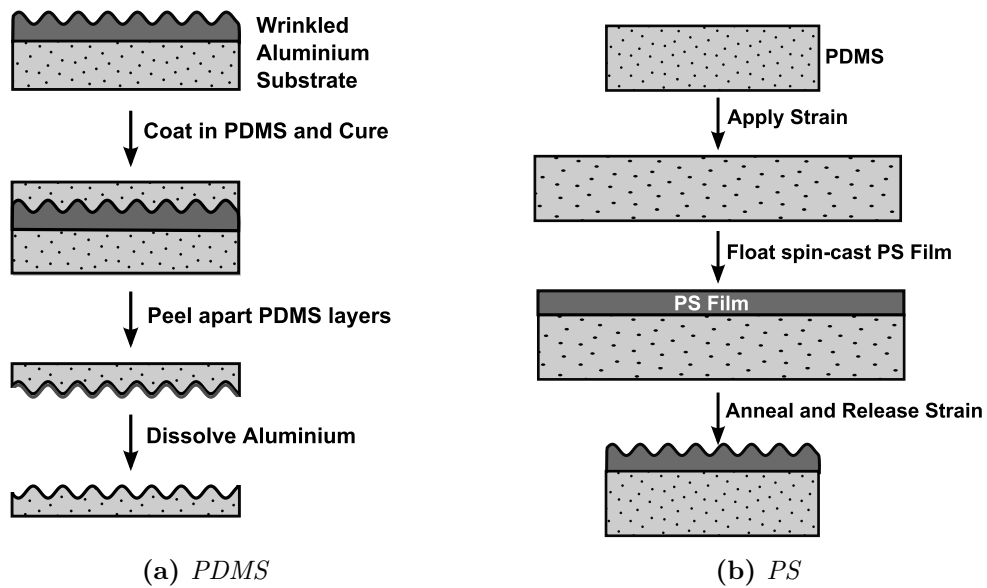These patterned polymer substrates were fabricated to avoid the issues de-

(a) *PDMS*   **(b)** *PS*

Figure 3.10: *The processes used to make wrinkled PDMS (Polydimethylsiloxane) and PS (Polystyrene) substrates. **(a)** Wrinkled aluminium substrates (Al on PDMS) were used as a mould for another layer of PDMS. Once applied, it was cured at $150°C$ before separating the two PDMS layers. Residue aluminium was dissolved using a sodium hydroxide solution. **(b)** Wrinkled PS substrates were made by floating a PS film onto a PDMS substrate that was under strain. After annealing, the strain was removed causing the PS to wrinkle.*

scribed in Section 3.4.1 for wrinkled metal substrates. However, this was largely unsuccessful. The PS substrates were very difficult to make and generally were formed with large defects in the polymer film. This was largely due to droplets of water getting trapped between the film and the PDMS substrate. There were also problems with the strain slowly relaxing and/or the substrate snapping whilst being heated in the oven. As is apparent from the micrograph in Figure 3.11, PS films were shown to crack in the same way as the metal substrates so did not remove the potential source of contamination. All of these issues meant this technique was of little value to this investigation and was not pursued further.

The PDMS substrates were more promising as they could be made with ease and produced repeatable structures. As they were moulded from the wrinkled aluminium substrates, although the structures of cracks were obviously still present, they do not provide a further source of contamination. As shown in
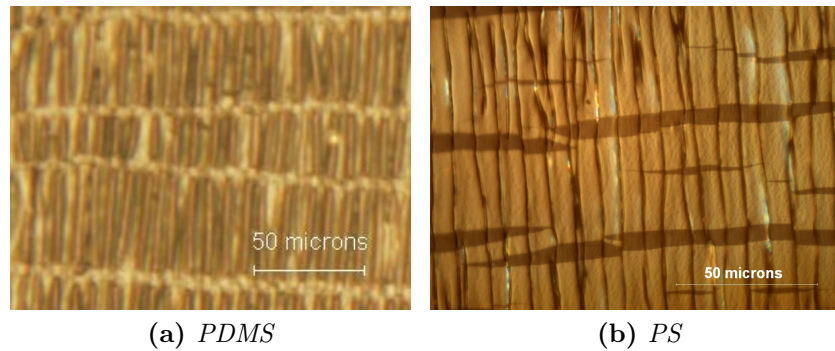
(a) *PDMS*   **(b)** *PS*

Figure 3.11: *Optical micrographs showing the structure of wrinkled polymer substrates fabricated using the two methods described. (a) shows PDMS (polydimethylsiloxane) moulded onto a wrinkled aluminium substrate. (b) shows a PS (polystyrene) film that was floated onto strained elastomer substrate. Relaxing the strain caused the wrinkling in the PS.*
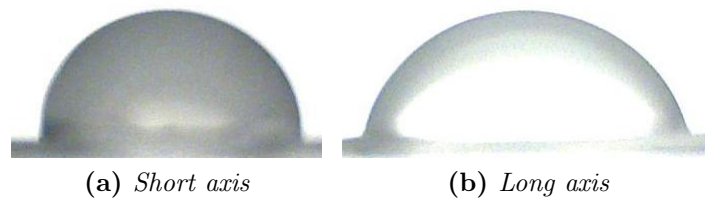

(a) *Short axis*   **(b)** *Long axis*

Figure 3.12: *Photographs showing the short and long droplet profiles of a $10\mu L$ droplet of water placed a PDMS substrate patterned with wrinkles. The substrate, using the process described in this section, was moulded from an aluminium/PDMS substrate (originally made by evaporating 100nm of aluminium onto PDMS under a 25% strain).*

Figure 3.12, droplets of water placed on these substrates did display obvious aspherical properties. They could therefore be used along with the methods described in Section 3.1 to measure the vibrational response of aspherical drops. Unfortunately, the positions of the resonant peaks in the vibrational speactra of the droplets placed on these surfaces were not repeatable between experiments. I therefore concluded that the PDMS substrates did not provide a cleaner alternative to using the wrinkled gold films.

3.4.3 Diffraction grating surface

It was decided that the simplest method of ensuring that the experiments were conducted on clean surfaces was to purchase a blazed, ruled diffraction grating (Thor Labs GR1325-10106). This surface, shown in the optical micrograph and AFM (atomic force microscopy) line profile in Figure 3.13, has a comparable structure to the wrinkled substrates discussed in sections 3.4.1 and 3.4.2. The grating is made up of periodic grooves running in a single direction with a periodicity of 10 microns and height of ∼3.5 microns. The only real difference to the wrinkled metal substrates (pictured in Figure 3.8) is that the line profile shown for the diffraction grating resembles a sawtooth waveform as opposed to the sinusoidal structure of the wrinkled surfaces. The diffraction grating was used in preference to the substrates made using the other procedures in this chapter because surface contamination appeared to be a large factor affecting the repeatability of the results and every indication showed this was a clean substrate.

When water droplets were placed on this surface, as with the wrinkled surfaces, the water was shown to spread anisotropically elongating the droplets. Photographs showing the short and long profiles of a 10μL water droplet placed on this surface are included in Figure 3.14. Looking at the shot profile, there is a subtle difference between how the droplet wets to the surface at each side of the drop. This is believed to be a result of the sawtooth waveform the grooves on the surface form.
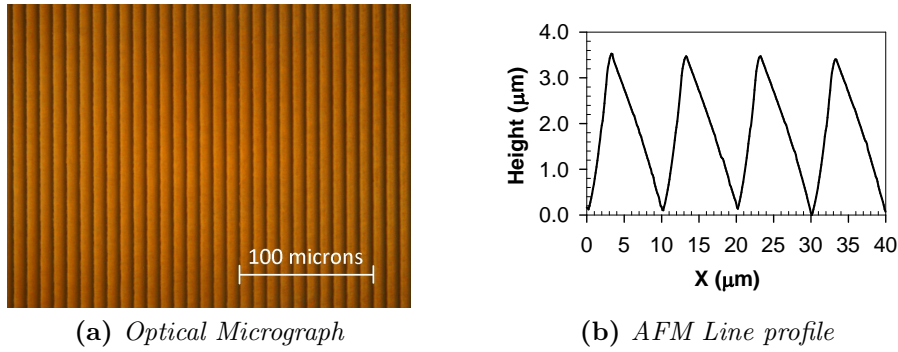
(a) *Optical Micrograph* **(b)** *AFM Line profile*

Figure 3.13: *The preferred substrate used in this study was a blazed diffraction grating with 10 micron periodicity shown in the above optical micrograph and height profile (obtained using AFM).*
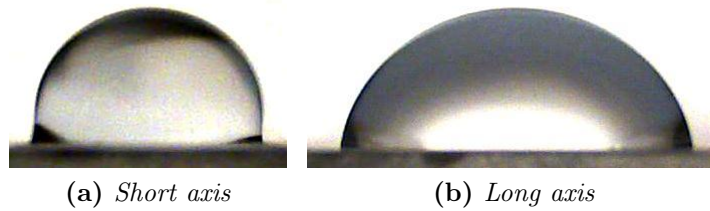

(a) *Short axis* **(b)** *Long axis*

Figure 3.14: *Photographs showing the short and long droplet profiles of a 10μL droplet of water placed the surface of the blazed diffraction grating.*

3.5 Wilhelmy plate technique for measuring surface tension

The Wilhelmy plate technique involves measuring the forces on a thin plate that is submerged into a liquid as is shown in Figure 3.15. A meniscus of liquid forms around the perimeter of the submerged plate which is subject to three forces. Firstly, the two forces acting downwards are the weight of the plate, W, and the force due to surface tension, $F_\gamma = 2\gamma(w+d)\cos\theta$. As shown in Figure 3.15, w and d are the width and thickness of the plate; $2(w+d)$ is therefore the perimeter of the plate. γ is the surface tension of the liquid and θ is the contact angle formed between the meniscus and the plate. These downward acting forces are countered by the buoyancy force resulting from the fact that the plate displaces liquid as it is submerged. This acts as an upthrust and is given by $F_{up} = \rho hwdg$ where h is the height to which the plate is submerged
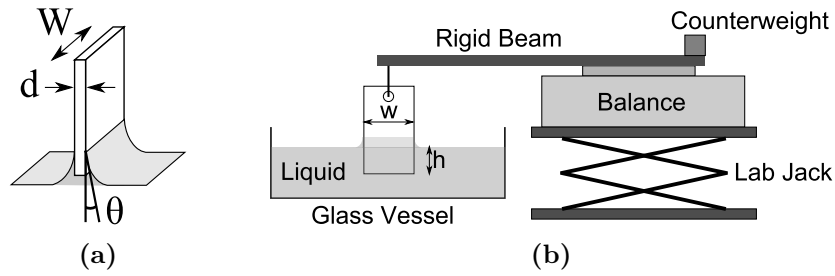
Figure 3.15: *Wilhelmy Plate Technique. **(a)** Illustration of the plate showing its dimensions and the contact angle formed between the plate and the meniscus. **(b)** A diagram of the apparatus used to measure the forces on a plate in order to determine the surface tension of the liquid*

and g is the acceleration due to gravity. The net downward force is therefore given by

$$F = W + 2\gamma(w + d)\cos\theta - \rho hwdg \tag{3.2}$$

Using the set-up shown in figure 3.15, the surface tension can be measured using the approach described by Erbil [69]. The plates used were home-made from Whatman chromatography paper (1Ch grade) which were cut by hand to have dimensions of 100mm×250mm×0.165mm. A hole was then stamped into the top allowing it to be suspended from the balance. Firstly, the plate was submerged into the liquid until capillary action had saturated the paper. The plate was then withdrawn entirely from the fluid and the balance zeroed thus eliminating the weight term in Equation 3.2. The plate was then resubmerged and withdrawn. As the plate was withdrawn, the maximum force read out from the balance, F_{max}, was recorded, at which point, the plate was at a depth of h=0 thus eliminating the buoyancy term in Equation 3.2. Finally, the use of chromatography paper as the plate meant the contact angle between the plate and liquid was ≈ 0 eliminating the cosine term. Equation 3.2 can then

be simplified to give only this maximum capillary force,

$$F_{max} \approx 2(w + d)\gamma \qquad (3.3)$$

from which γ was calculated. Assuming the contact angle to be zero is an approximation, albeit a common one, meaning the measured surface tensions could be slightly higher than predicted. If very accurate measurements of γ were required, one would need to take θ into account. However, for the purposes of this investigation, other variables such as surface contaminants were shown to provide much greater uncertainties in the measurements.

Chapter 4

Surface Tension of Water

A knowledge of the surface tension of water underpins many of the measurements and theories that are included in this work. In this section, we therefore aim to measure the surface tension of water using well established methods in order to aid the analysis of the data presented in the following chapters.

4.1 Wilhelmy plate technique

This simple technique allows the surface tension of a liquid to be approximated by submerging a plate into a bath of the liquid. In this case, the plates used were hand-cut rectangles of Whatman chromatography paper (1Ch grade). As described in Section 3.5, the balance of the forces acting on the plate, including gravity, surface tension and buoyancy forces, were measured using a digital balance. Although measurements can be taken in a number of ways using this approach [69], our method involved saturating the chromatography paper with the liquid being measured and positioning the paper so that its bottom edge sat on the surface of the liquid. Subtracting the weight of the saturated paper from the force read from the balance gives the "maximum force" described
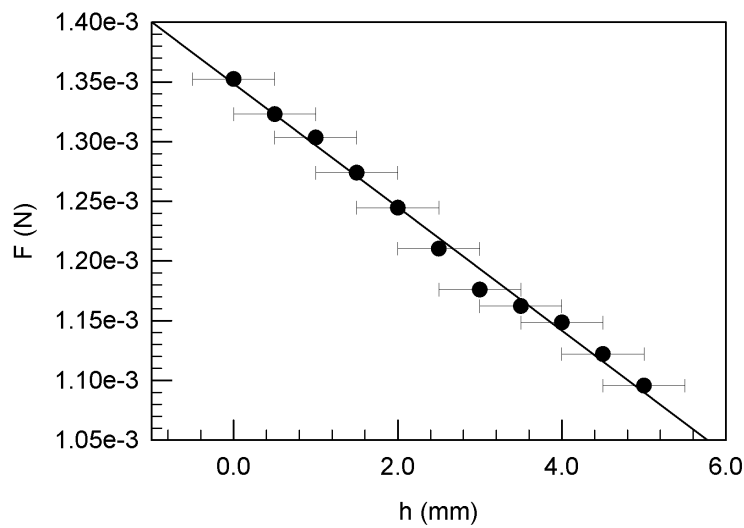
Figure 4.1: *Plot showing how the downward force on a Wilhemy plate varied as the plate was submerged into a bath (with diameter 5cm) of water. h=0 is defined as the surface of the liquid.*

in equation 3.3. From this, the surface tension can be approximated if the dimensions of the plate are known.

Deionised water (from an ELGA purification unit) was placed in a glass dish that had been thoroughly cleaned using chloroform. The plate, attached to the balance, was placed on the surface of the water (defined as h=0). Once saturated, the plate was slowly submerged and the force on the plate due to capillary and buoyancy forces was calculated by subtracting the weight of the saturated plate. A plot of this is shown in Figure 4.1, where as expected, the force varies linearly as the plate is submerged deeper into the liquid bath. If we take the h=0 value for the force (the y intercept), equation 3.3 gives us $\gamma = 65 \pm 1 \text{mNm}^{-1}$. Literature values for the surface tension of water are $\gamma = 72.0 \text{mNm}^{-1}$ at 25°C and $\gamma = 72.8 \text{mNm}^{-1}$ at 20°C [58].

The value of F_{max} was obtained numerous times for water. Each time, a new plate and a fresh water sample were used. The glassware holding the liquid was thoroughly cleaned using chloroform prior to use. The complication was that the surface tension appeared to decrease over time which is likely to be an effect of contamination of the water/air interface from organic molecules in

Table 4.1: *Values of surface tension for various liquids measured using the Wilhelmy plate technique compared with values from the literature [71].*

Liquid	Surface Tension γ (mNm^{-1})	
	Measured	Literature value at 25°C [71]
Water	60 ± 3	72
Formamide	58 ± 1	57
Chlorobenzene	33 ± 1	33
Hexadecane	27 ± 1	27
Methanol	24 ± 1	22

the air. If the measurements were taken as quickly as possible, the measured values of surface tension fell between the values of $\gamma \approx 65\text{mNm}^{-1}$ and $\gamma \approx 74\text{mNm}^{-1}$. If the measurements were taken after waiting ~ 10 minutes, the force on the plate was consistently measured to correspond to a surface tension of $\gamma \approx 60 \pm 3\text{mNm}^{-1}$. These findings are consistent with those of Henderson and Miles who observed dramatic decreases in measurements of surface tension values after 1min of being exposed to ambient conditions [70].

The value of $\gamma \approx 60 \pm 3$ mNm^{-1} is given as an approximate value because of the approximations made in the calculation. These include having a contact angle between the plate and the bath of liquid of zero and the value of F_{max} occurring at $h = 0$. The error stated is the standard error calculated from taking repeat measurements.

The same experiment was done for various other liquids to check the validity of the technique. Table 4.1 shows that the values obtained for these other liquids agree with those from the literature. This is likely to be because these lower surface tension liquids have liquid/air interfaces that are less susceptible to surface contamination when compared to water/air interfaces.

4.2   Diamagnetic levitation

If placed in a large enough magnetic field, diamagnetic materials such as water produce a magnetic field opposing the applied field. This repulsive force can be used to counter the effects of gravity creating a stable levitation point at which the two forces are balanced. In these experiments, a vertical bore super-conducting magnet was used to create such a levitation point where droplets of deionised water from an ELGA purification system were suspended. The strength of the magnetic field at this levitation point was $\sim$ 17T. Once levitated, the methods described in Section 3.3 were used to measure the vibrational response of the drops: Laser light was focussed through the drop and when the drop was perturbed by a puff of air, the resulting variations in the shape of the drop caused fluctuations in the light incident on a photodiode. The time dependent voltage from the photodiode was then Fourier transformed to give the vibrational spectra of the drops.

Vibrational spectra were collected for a range of drop sizes with masses between 0.20g and 2.44g corresponding to radii of r=3.6mm and r=8.4mm. For each drop, a number of spectra were collected that could be compared against eachother. An example of the data collected for a 0.94g (r=6.1mm) droplet is shown in Figure 4.2. The peaks visible in the spectra at 8.5Hz, 16.1Hz and 24.9Hz correspond to the l=2, l=3 and l=4 oscillations. Higher order peaks (some of which are just about visible at this magnification) are present but with a relatively very small amplitude.

The frequency of these peaks were plotted as a function of $r^{-3/2}$ and as predicted by Rayleigh's equation (equation 2.5),

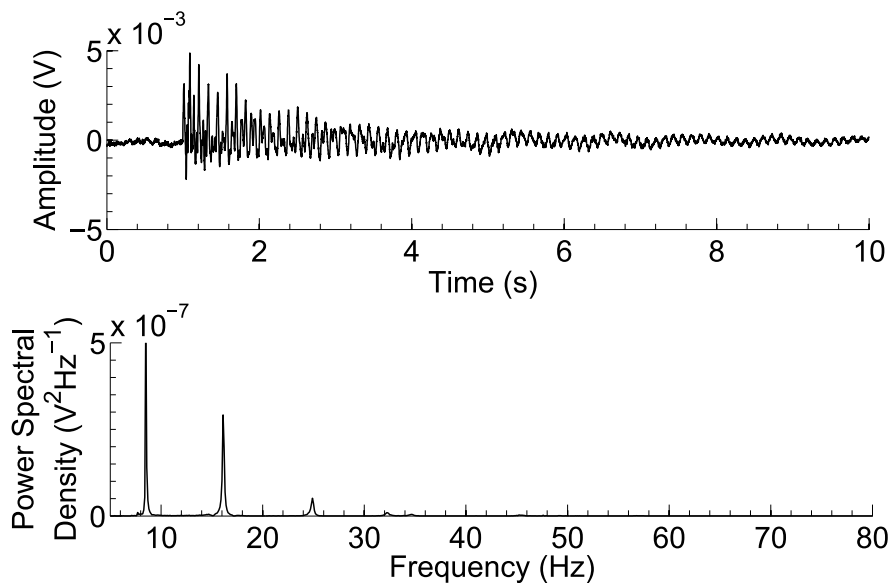$$f = \frac{1}{2\pi} \left(\frac{l(l-1)(l+2)\gamma}{\rho r^3} \right)^{1/2} \tag{4.1}$$

Figure 4.2: *A set of data collected for a magnetically levitated 0.94g water droplet with a radius of r=6.1mm. The top figure shows the time dependent voltage from the photodiode which was Fourier transformed to produce the vibrational spectra shown in the bottom figure.*

each mode forms a straight line. This is shown in Figure 4.3a and the l=2 mode is shown in detail on its own plot in Figure 4.3b. Using the Rayleigh equation, the gradient of the l=2 line was used to obtain an effective surface tension of $\gamma_{eff.} = 70.0 \pm 1.2$ mNm^{-2} (the error bar was calculated using 95% confidence bounds). This does not represent a true surface tension because the diamagnetic forces act as a restoring force slightly increasing frequencies measured. This can be corrected for using the methods described by Hill et al. [13] to give $\gamma = 68.5 \pm 1.2$ mNm^{-2}(assuming there is no error in the correction)[1].

This value is significantly higher than that measured using the Wilhelmy plate technique. This could be because the system used for the levitation experiment is less susceptible to contamination. Even though the drops were exposed to the air for a significantly longer period of time (>30mins), the experiments

---

[1]This correction required modelling the magnetogravitational potential inside the bore of the magnet. These computations were kindly done by Dr. Richard Hill, School of Physics and Astronomy, University of Nottingham. The calculation performed using the data extracted from the computations assumed the potential was spherical (quadrupole and higher order corrections were not taken into account).

were isolated from ambient conditions by the enclosure discussed in Section 3.3. This idea is based on the findings of Henderson and Miles who found that the act of enclosing their experiments in this way meant no noticeable changes in surface tension were detected over a 3 hour period [70].
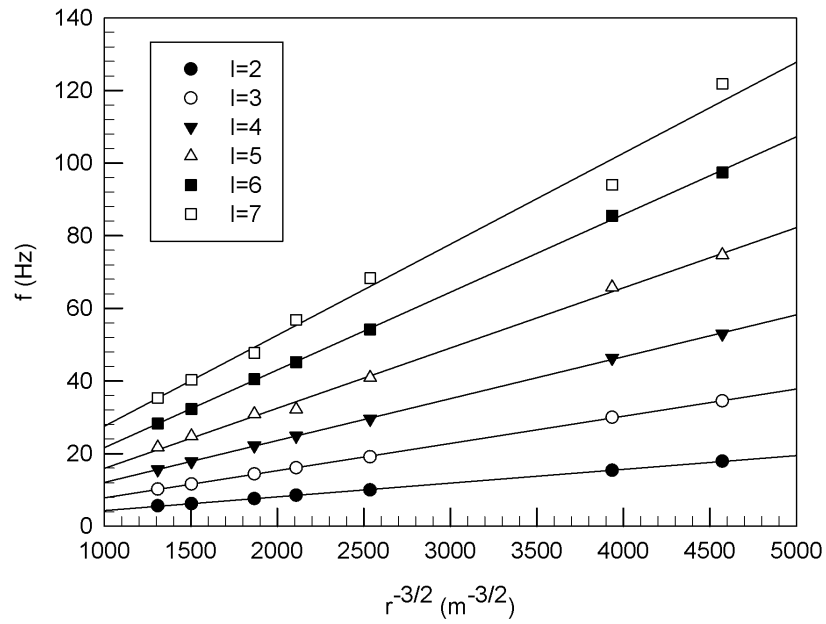
(a) *All Modes*

(b) *l=2 mode*

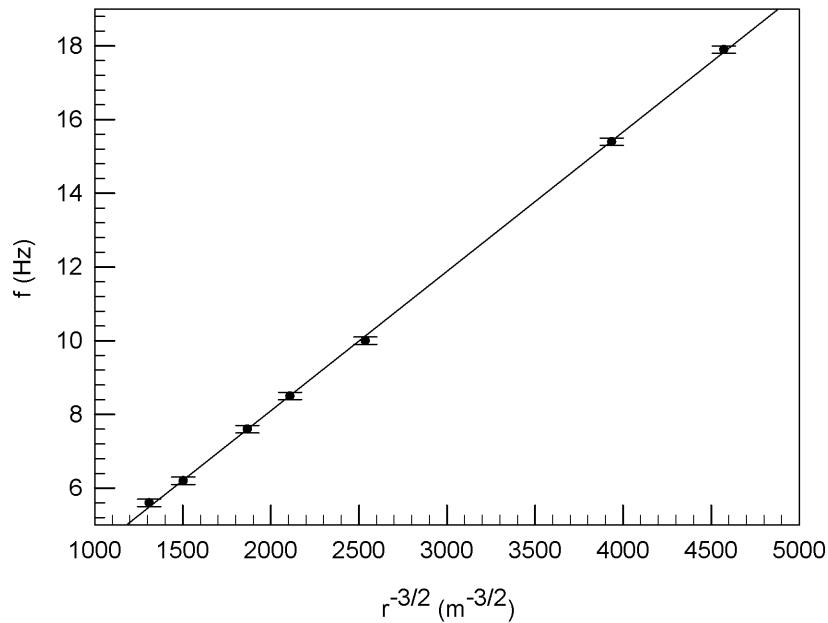**Figure 4.3:** *The variation of frequency f with $r^{-3/2}$ where r is the radius of the levitated water drop.* **(a)** *shows the data for the first 6 allowed modes.* **(b)** *shows the $l = 2$ mode from which an effective surface tension of $\gamma_{eff.} = 70.0 \pm 1.2 mNm^{-2}$ was calculated from the gradient of the solid line using Rayleigh's equation (equation 2.5).*

Chapter 5

Vibration of Spherical and Aspherical Sessile Droplets

As discussed previously, the vibrational modes of sessile drops have been studied by a number of authors including Strani [46] [47], Celestini [48], Vukasinovic [2] and Mettu [68]. However, the most relevant work to this study is from Sharp [10] [12] and Noblin [50] [4] whose ideas are used extensively. This chapter aims to use the work of these authors to investigate the vibrational properties of aspherical sessile drops produced by exploiting the anisotropic wetting properties of patterned surfaces. In order to carry out this investigation, spherical drops were also studied. The resulting data could not only be directly related to the literature but also allowed comparisons to be made between the spherical and aspherical cases. Furthermore, the study of spherical caps provided a simpler groundwork from which to develop the experimental methods used and provided evidence supporting the validity of these methods.

This chapter also presents ideas about how the dispersion relation for capillary-gravity waves on a liquid bath can be applied to droplets. Specifically, we focus on the term in the equation compensating for the bath being of a finite rather

than infinite depth and explore Noblin's approximation of modelling the depth of the bath as the average height of the droplets.

We also use the vibration of sessile droplets as a measurement technique for the surface tension and viscosity of water. These measurements are conducted not only as a demonstration of a potential application of the techniques used, but also as a tool allowing the comparison of the data collected to that predicted by the models discussed previously in the earlier chapters of this thesis.

5.1 Spherical droplets

5.1.1 Experimental details

The experimental method described in Section 3.1 was used to measure the vibration response of spherical cap water droplets placed on flat PDMS (Poly-dimethylsiloxane) substrates. The PDMS substrates were made using Sylgard "184 Silicone Elastomer" which, once mixed with its cross linking agent (10:1 ratio by weight) was spread over a glass microscope slide and annealed at 150°C. Small, microlitre sized volumes of LC-MS (liquid chromatography-mass spectrometry) grade deionised water (Sigma Aldrich) were placed onto the substrates using a micropipette.

As described in Section 3.1, the water droplets were perturbed using a puff of nitrogen gas and the vibrational response was measured by scattering laser light off the drops onto a photodiode. For each set of data collected, the voltage from the photodiode was recorded for 5 seconds at a sample rate of 1000Hz using a National Instruments USB-6008 data acquisition card. Fourier transformation of this time dependant data gave vibrational spectra with a resolution of 0.2Hz. An example set of data is shown in Figure 5.1 for a 10μL
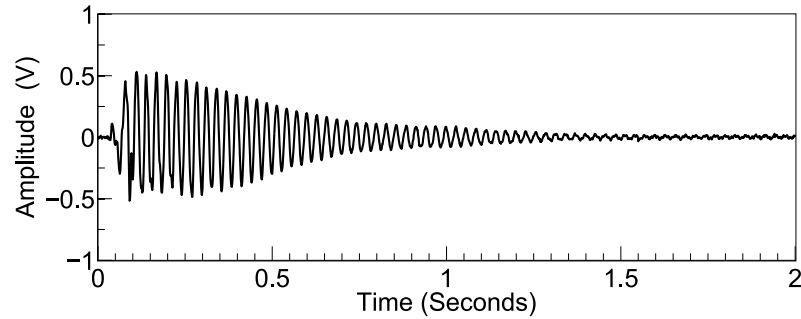
(a) *Photodiode Signal*
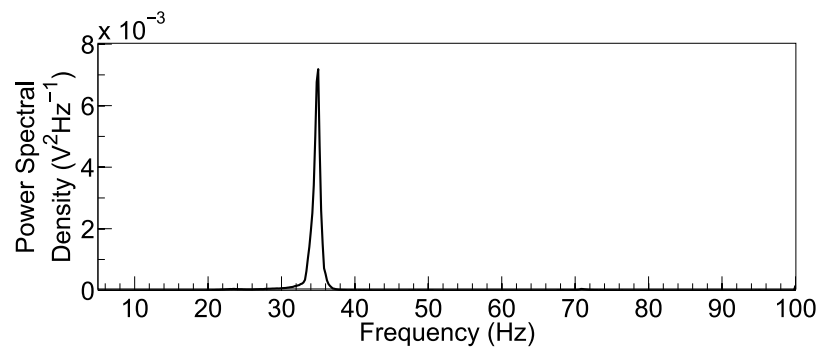
(b) *Vibrational Spectra*
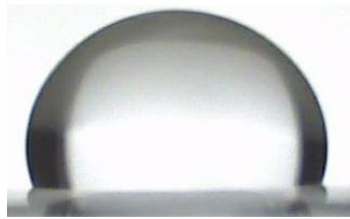
(c) *Photograph of Drop*
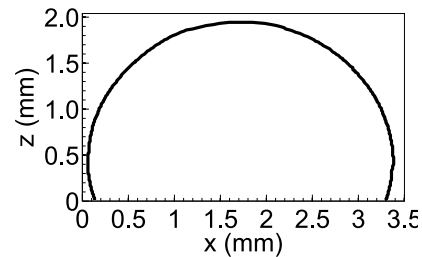
(d) *Vibrational Spectra*

Figure 5.1: *Example set of data for a 10μL droplet of water on a PDMS substrate.* **(a)** *shows the time dependent voltage fluctuations collected from the photodiode which was fourier transformed to give the vibrational spectra in* **(b)**. *The peak shown, corresponding to the n=2 mode, is at 35Hz with a full width at half maximum of 0.9Hz. The photograph of the droplet* **(c)** *was used to extract the profile of the drop shown in* **(d)**

droplet of water on a PDMS substrate. The time dependent data was Fourier transformed using Matlab to give the vibrational spectra shown with a single peak, corresponding to the n=2 mode, at $f = 35 \pm 0.2$ Hz with a full width at half maximum (FWHM) of $\Delta F = 0.9 \pm 0.28$ Hz. This is the fundamental resonance as the n=1 mode is not permitted due to the fact the liquid is incompressible.

Once this data was collected, a photograph was taken of the droplet profile using a Phillips SPC100NC webcam. This was processed in Matlab in order to measure profile length of the drop. Figure 5.1 includes shows the photograph taken of the 10μL droplet discussed above and a plot of the profile extracted from the photograph. From this, the profile length was calculated to be $L = 6.1 \pm 0.1$ mm.

5.1.2   Analysis of the resonant frequencies and measurement of surface tension

Data was collected for drops with volumes between 0.2μL and 25.0μL which have profile lengths ranging from 4.1mm to 7.9mm. The n=2 resonant peaks for this range of drop sizes fell between 24Hz and 65Hz with widths between 0.5Hz and 2.0Hz. Figure 5.2 shows the square of these frequencies, f^2, plotted as a function of the inverse of the profile length cubed, L^{-3}. As predicted by equation 2.12, this is a linear relationship allowing the surface tension of the liquid to be calculated from the line of best fit. Assuming the density of water to be $998 kgm^{-3}$ [57] and $\alpha = 0.81$ (Sharp's scaling factor [10] discussed in Section 2.3.3), equation 2.12 gives $\gamma = 65.5 \pm 1.0$ mNm^{-1} (error bar calculated from 95% confidence bounds).

The relative error in L is $\sim 2\%$ which is reflected in the error bars shown in Figure 5.2. This is the uncertainty obtained for the aspherical drops discussed
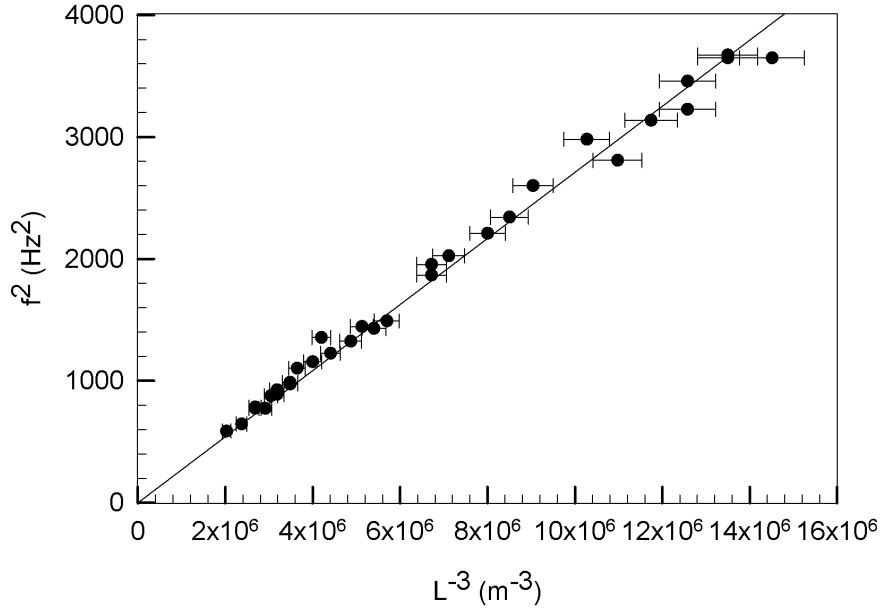
Figure 5.2: *Plot showing the position of the n=2 resonant frequency peaks in the vibrational spectra collected for droplets of water on PDMS (polydimethylsiloxane). The square of the frequency, f^2 is plotted as a function of L^{-3} where L is the profile length of the drop. Using Equation 2.12 and the gradient of the line of best fit shown, the surface tension was calculated to be $\gamma = 65.5 \pm 0.1$ mNm^{-1} (assuming $\alpha = 0.81$ [10]).*

in Section 5.2.3. The uncertainty in the frequency is 0.2Hz (limited by the resolution in the Fourier transform of the time dependant data) which gives error bars that are negligible when considering the uncertainty derived from the errors in L. Errors in the gradient of the fit used to find γ were calculated from the 95% confidence bounds obtained using the "curve fitting toolbox" in Matlab (Mathworks).

As described in Section 2.3.3, Noblin modelled these oscillations as capillary waves on the surface of a liquid bath of depth $\bar{h}$ where $\bar{h}$ is the average height of the drop [50]. We recall that

$$\alpha = \sqrt{\tanh\left(\frac{n\pi\bar{h}}{L_i}\right)} \tag{5.1}$$

is the term in the dispersion relation for capillary waves (equation 2.11) that compensates for the bath of liquid being of finite (rather than infinite) depth. Noblin determined α by approximating the average height of a drop to be the ratio of it's volume and basal area. However, for the case of a spherical cap, analytical expressions for $\bar{h}$ and thus α can be found. There are two methods for calculating the average height. The first method weights $\bar{h}$ by volume and gives

$$\alpha = \sqrt{\tanh\left(\frac{n\pi}{4\theta}\left(\frac{-\cos^4\theta + 6\cos^2\theta - 8\cos\theta + 3}{\cos^3\theta - 3\cos\theta + 2}\right)\right)} \qquad (5.2)$$

where θ is the contact angle of the drop. This equation was derived by defining contours of constant height on the surface of a spherical cap with a "tube like" volume element beneath them (see Figure A.1 at the start of Appendix A.1). In this case, the average height of the drop was calculated by weighting the height of each contour by the size of it's associated volume element. The second method takes a similar approach but weights the height of the contours by the area of the surface enclosed between them. This gives

$$\alpha = \sqrt{\tanh\left(\frac{n\pi}{4\theta}\left(\frac{\cos^2\theta - 2\cos\theta + 1}{1 - \cos\theta}\right)\right)} \qquad (5.3)$$

The full derivation of both of these expressions are included in Appendix A.1.

These solutions are given as a function of contact angle rather than profile length for convenience. They can also be expressed in terms of L because for a spherical cap as $L = 2R\theta$ where R is the radius of curvature. However, this makes the expressions much more complex and adds an additional variable, R. Since the contact angle remains approximately constant for a liquid on a given substrate, leaving it in terms of θ allows us to treat α as a constant whose
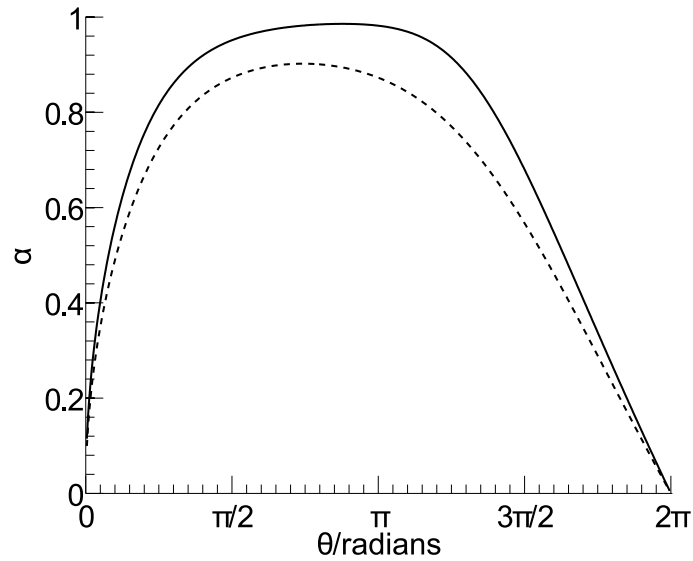
Figure 5.3: *Plot of theoretical values of α against contact angle for a spherical cap. α, defined in equation 5.1 is a function of the average height of the drop, $\bar{h}$ which has been evaluated for the case of a spherical cap using two methods. The solid line shows α as a function of the contact angle, θ, when $\bar{h}$ was weighted by volume and the dashed line when $\bar{h}$ was weighed by surface area.*

value is easily measured for a liquid/substrate combination.

Figure 5.3 shows a plot of both equations 5.2 and 5.3. It is apparent that the two approaches described give very different solutions, and considering how sensitive equation 2.12 is to small changes in α, we aim to determine which is the correct method. However, this is not a trivial problem to solve. It is also quickly apparent that these solutions do not correlate well with the experimental work of Sharp and his colleagues because these analytical solutions have a very strong contact angle dependence which was not present in Sharp's data.

If we use these solutions to calculate γ for this dataset, assuming a contact angle of 110° for water on PDMS (as is evident from the photographs), equations 5.2 and 5.3 give values of $\alpha = 0.97$ and $\alpha = 0.89$ respectively. These in turn give surface tension values of $\gamma = 45.7 \pm 1.0$ mNm^{-1} and $\gamma = 54.1 \pm 1.0$ mNm^{-1} (error bars calculated using 95% confidence bounds).

None of the three possible values for the surface tension of water presented provide a good match with the literature value of $\gamma = 72.8$ Nm^{-1} at 20°C [56]. Surface tension is very weakly dependent on temperature - in the temperature range of 15°C - 25°C, the surface tension varies between 73.5mNm^{-1} and 72.0mNm^{-1} [56]. All the data collected was taken well within this temperature range so the effect of temperature is discounted. The most likely explanation for measuring lower values of γ than the literature value is contamination of the liquid's surface. The values for γ obtained using Sharp's scaling factor are within the ranges measured using the Wilhelmy plate technique in Section 4.1 for deionised water. However, the values for γ obtained using the values of α calculated here are not. This perhaps implies that Noblin's approach (discussed in Section 2.3.3) of approximating the depth of the bath of liquid to be the average height of the drop [50] is too simplistic. Using Sharp's scaling factor could therefore be the most valid approach as it was determined experimentally meaning it is independent of any mathematical models or approximations.

The data presented in this section was collected using the same water and the same substrate on multiple occasions. The fact the data falls onto the same line shows that the technique gives repeatable results. However, when different substrates and water samples were used, given the same value of α, the gradients of the fitted lines varied dramatically. This again suggests that the water is likely to be suffering from contamination from either the supply of water or from the substrates that the water was placed on.

5.1.3 Analysis of damping and the estimation of viscosity

Assuming that bulk viscous damping is the dominant source of damping in the system and given that the full width at half maximum of the resonant

peaks, Δf, is equivalent to the damping coefficient in an exponentially decaying signal, equation 2.14 predicts a linear relationship between Δf and L^{-2}. Figure 5.4 shows a plot of Δf as a function of L^{-2} and although there is a clear positive correlation, it is not clear the relationship is linear due to the large amount of scatter in the data. This could be a result of the error bars in both directions being so large. The absolute error in the widths, ± 0.28Hz, is derived from the resolution in the frequency spectrum (0.2Hz) whilst errors in L have the same 2% relative error mentioned above. Whilst the error from the resolution of the Fourier transform is small when considering the position of the resonant peaks, the peaks have a width of $\Delta f \sim 1$ Hz making ± 0.28Hz a significant error. Despite this, the positive correlation is enough for us to make an estimation of the viscosity of the liquid. Assuming the density of water is $\rho = 998$ kgm^{-3} [57], the gradient of the line of best fit through all the data (the solid line in Figure 5.4) gives $\eta = 0.52 \pm 0.11$ mPa.s (95% confidence bounds).

It is possible to argue from looking at this plot that the data for small droplets appears to be skewing the line of best fit away from the relatively linear region for larger drops ($L^{-2} \gtrsim 50 \times 10^3 m^{-2}$). The dashed line on this plot shows a line of best fit that is forced through the origin with the data above $L^{-2} = 50 \times 10^3$ m^{-2} excluded. Analysis of the gradient of this line gives $\eta = 0.88 \pm 0.04$ mPa.s (95% confidence bounds). It is stressed that we have no justification for ignoring these results as they are not individual outliers - small drops were consistently having this effect on the measured viscosity. A number of factors, such as evaporation, make the measurement of small drops difficult. It is also possible that different damping mechanisms become more dominant when the size of the drop is reduced to such small volumes.

The literature value of the dynamic (absolute) viscosity of water at 20°C is $\eta = 1.00$ mPa.s [72] which is a close match to the value of $\eta = 0.88 \pm 0.04$ mPa.s obtained here by excluding the points in Figure 5.4 that were skewing
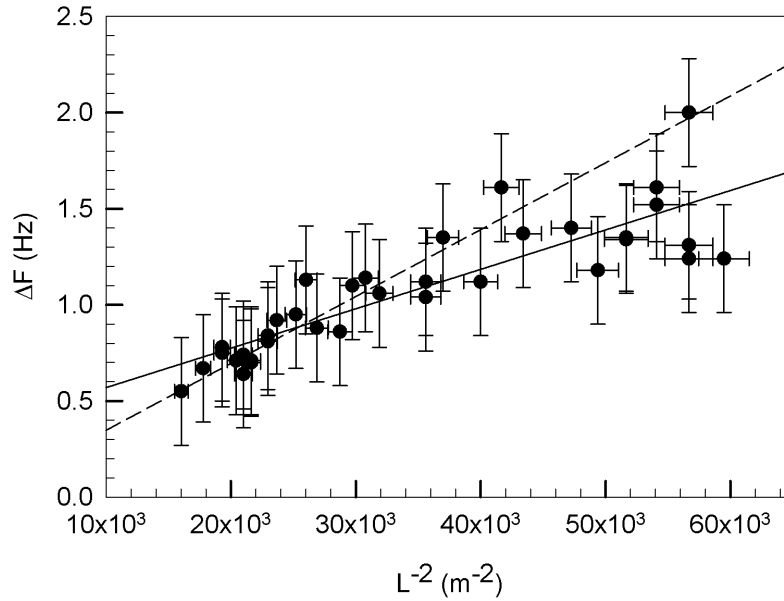
Figure 5.4: *Plot showing the widths (full width at half maximum) of the n=2 resonant frequency peak in the vibrational spectra collected for droplets of water on PDMS (polydimethylsiloxane). The widths, ΔF are plotted as a function of L^{-2} where L is the profile length of the drop. The solid line shows a line of best fit calculated from all the data and the dashed line shows a fit forced through the origin where the small drops (above $L^{-2} = 50 \times 10^3 m^{-2}$) were excluded. Using Equation 2.14 and the gradient of the dashed line, the viscosity of the liquid was estimated to be $\eta = 0.88 \pm 0.04$ mPa.s*

the line of best fit. It is also worth noting that the expression used to calculate η (equation 2.14) is independent of α. This gives further credibility to the technique and implies that some of the issues discussed above originate from a potentially over-simplistic model. If all of the data is considered, the value of measured viscosity falls below the literature value by around a factor of 2. Although not a perfect match, it is a comparable factor to that observed by Sharp [12].

5.2 Aspherical droplets

5.2.1 Experimental details

The technique of studying the vibrational spectra of spherical caps was extended to examine the modes of vibration in aspherical droplets. As discussed in Section 2.3.5, surfaces patterned with periodic grooves display anisotropic wetting properties which can be exploited to produce sessile droplets with an elongated shape. Section 3.4 outlines some of the processes used to produce these surfaces based around the ideas of wrinkling metal and polymer films. However, the surface of choice was that of a blazed diffraction grating (Thor Labs, GR1325-10106); a brief discussion of which, including images and line profiles of the surface, can be found in Section 3.4.3. The diffraction grating was the preferred surface because, although an extensive amount of data was collected using wrinkled metal and polymer surfaces, the results were not entirely repeatable. It was suspected these issues were a result of contaminants produced in the fabrication processes that influence the surface tension of any liquid placed on the surfaces. As discussed, the most likely contaminant is residual monomer and cross linking agent from the PDMS substrates. As shown in this section, the suspected contamination issues linked to these alternative substrates were not present when the diffraction grating was used.

The technique outlined in Section 3.1 was used to extract vibrational spectra for droplets of water placed on the surface of the diffraction grating. For each set of data collected, the voltage from the photodiode was recorded for 5 seconds at a sample rate of 1000Hz using a National Instruments USB-6008 data acquisition card. An example set of data for a 5μL droplet is shown in Figure 5.5. This droplet was observed to spread in such a way that gave basal radii of 1.6mm/1.1mm and profile lengths of 4.8mm/4.1mm along the major/minor axis of the drop. As predicted in Section 2.3.5, the vibrational

(a) *Photodiode Signal*

(b) *Vibrational Spectra*
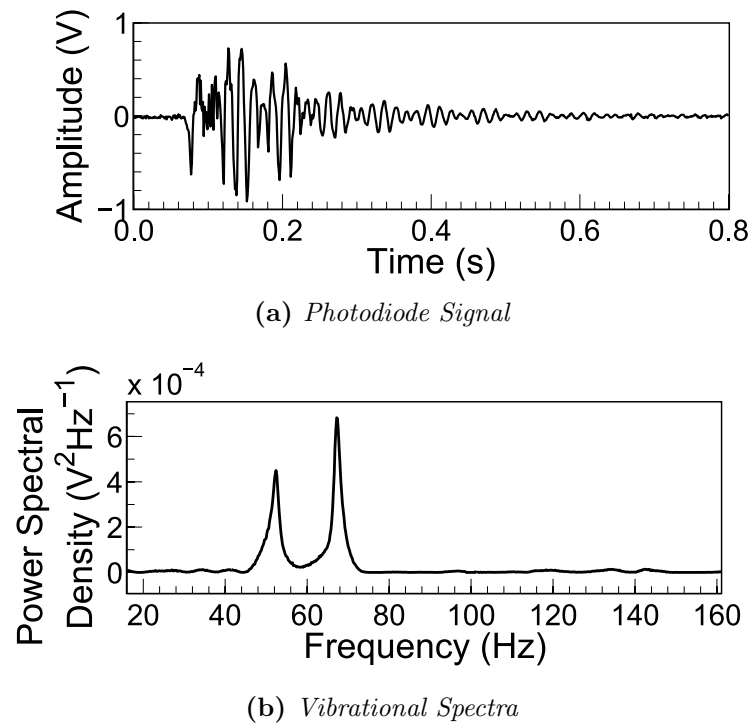
(c) *Long Axis*
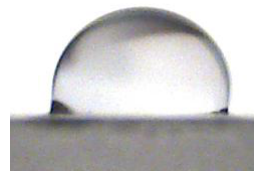
(d) *Short Axis*

Figure 5.5: *Example set of data for a 5μL droplet of water on the surface of the blazed diffraction grating.* ***(a)*** *shows the time dependent voltage fluctuations collected from the photodiode which was fourier transformed to give the vibrational spectra in* ***(b)***. *The two peaks shown correspond to the splitting of the n=2 mode into oscillations along the two profile lengths calculated from the photographs shown in* ***(c)*** *and* ***(d)***. *The lower/higher frequency peak corresponds to the oscillations about the long/short axis.*

spectra shows two distinct but closely separated peaks corresponding to n=2 standing wave states along the long and short profiles (major and minor axes) of the drop. The lower frequency peak at 52.4 ± 0.2 Hz corresponds to the oscillations around the long axis and the higher frequency peak at 67.2 ± 0.2 Hz to the oscillations around the short axis of the drop. The obvious envelope in the photodiode signal, representing the beating of the 2 modes, demonstrates that there are 2 frequencies present. The higher frequency oscillations visible in the photodiode signal at ~ 0.1s represent the higher order ($n \geq 3$) modes of oscillation which decay away rapidly.

5.2.2   The orientation of the droplet

It was quickly apparent that the relative heights of the two peaks in the spectra could be controlled by changing the orientation of the droplet relative to the direction of the laser beam. The diffraction grating, with a 15µL drop of water on its surface, was placed in the centre of a rotation stage with the long axis of the drop in the path of the laser beam as shown in Figure 5.6a. Vibrational spectra of the drop were collected every 10° as the drop was rotated through 90°. This was repeated three times for the same droplet. At the 90° position, as shown in Figure 5.6c, the long axis of the drop was perpendicular to the path of the laser beam. Figure 5.7a shows how the mean ratio of the two peak heights varies as the drop was rotated. The insets in this figure show examples of the vibrational spectra collected at 20°, 50° and 90°. The positions of the two peaks visible in the spectra are shown as a function of angle in Figures 5.7b and 5.7c for the first repeat. The slight increase in frequency is a result of drop evaporation slowly reducing the size of the droplet and hence the profile lengths of the major and minor axes. The further two repeats showed comparable evaporation rates.

An important conclusion to draw here is that when one of the droplet's primary

axes was perpendicular to the laser beam, only the resonant peak corresponding to that axis was visible in the vibrational spectra. As the drop was rotated, the ratio of amplitudes was observed to vary monotonically from a situation where one peak was dominant to a situation where the other peak was dominant. Meanwhile, the frequencies of both peaks remained approximately the same. These two observations support the idea that the peaks observed in the vibrational spectra correspond to vibrations along the profile lengths of the major and minor axes of the drops.

During these experiments, the position of the photo diode was kept constant as it was also apparent that the position of the photodiode in the cone of scattered light had a slight effect on the peak amplitudes. However, compared to the orientation of the drop, this effect was relatively minor. Although this may be a factor as to why some of the points in Figure 5.7a appear to be slightly off the position that surrounding points would imply, the effect is too minor to explain the overall observations in the spectra when the drop was rotated.
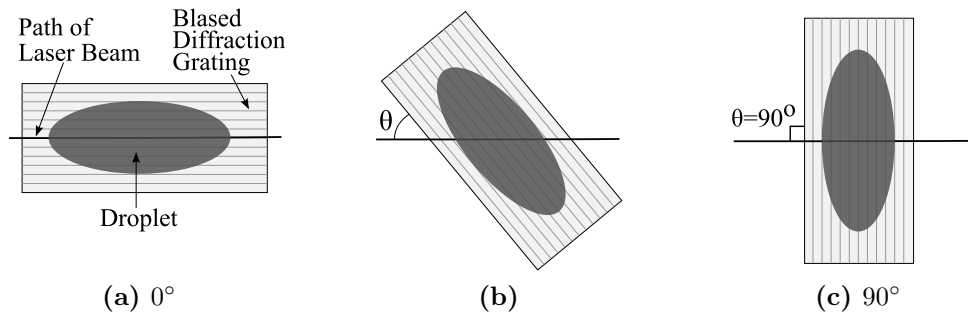

(a) 0°   **(b)**   **(c)** 90°

Figure 5.6: *Diagrams showing how the drop was oriented relative to the laser beam for the rotation experiments. The definitions of 0° and 90° are shown.*

(a) *Ratio of peak heights*

(b) *Short axis peak positions*

(c) *Long axis peak positions*
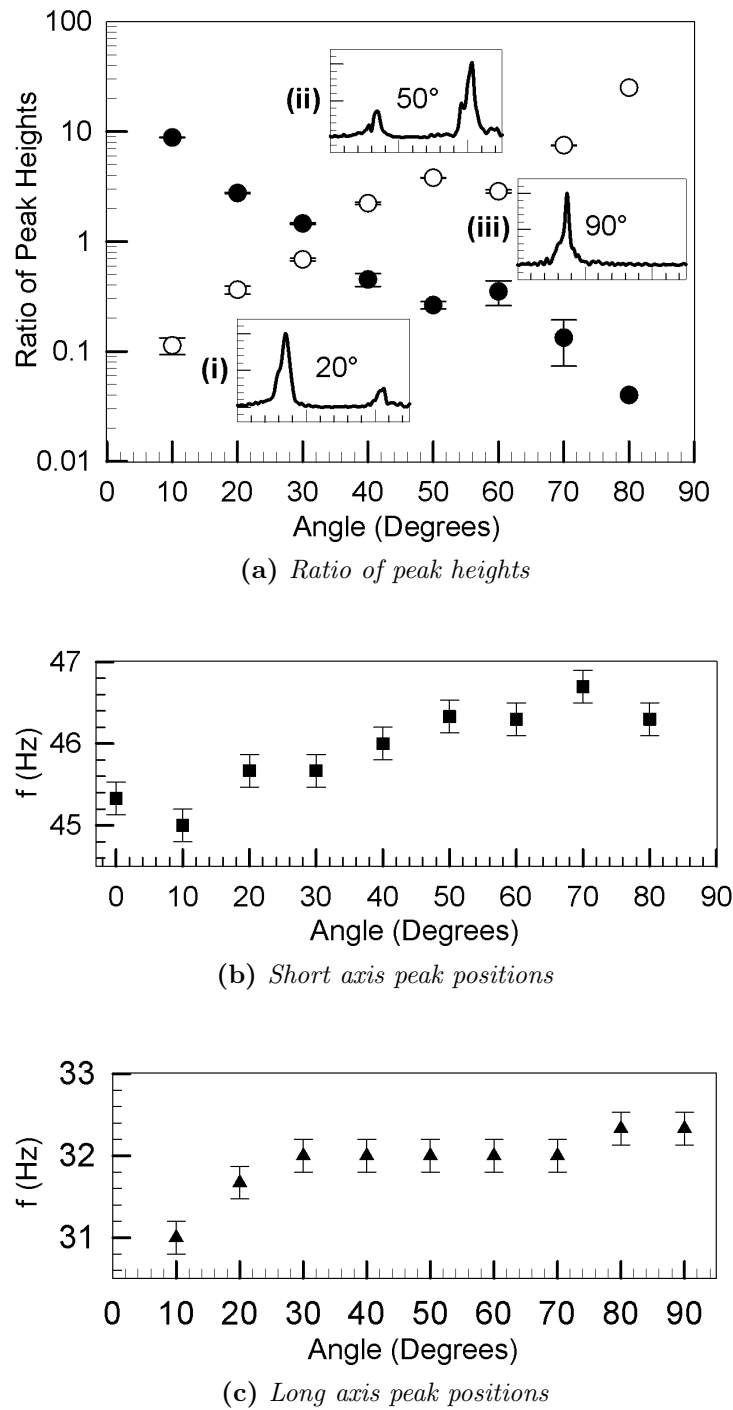
Figure 5.7: *A drop was rotated through 90° with a spectra of the oscillations acquired every 10°. This was repeated three time for the same drop.* **(a)** *shows the mean ratio of the two peak heights plotted as a function of the angle between the drop's major axis and the laser beam. The insets* **(ii)**, **(ii)** *and* **(iii)** *show examples of the normalised spectra collected during the first repeat at 20°, 50° and 90° respectively.* **(b)** *and* **(c)** *show how the position of the high and low frequency peaks respectively shifted during the first repeat. The increase in frequency as angle increases is the effect of evaporation decreasing the drop volume. The further two repeats showed comparable evaporation rates.*

Figure 5.8: *Plot showing the position of the n=2 resonant frequency peaks in the vibrational spectra collected for aspherical droplets of wat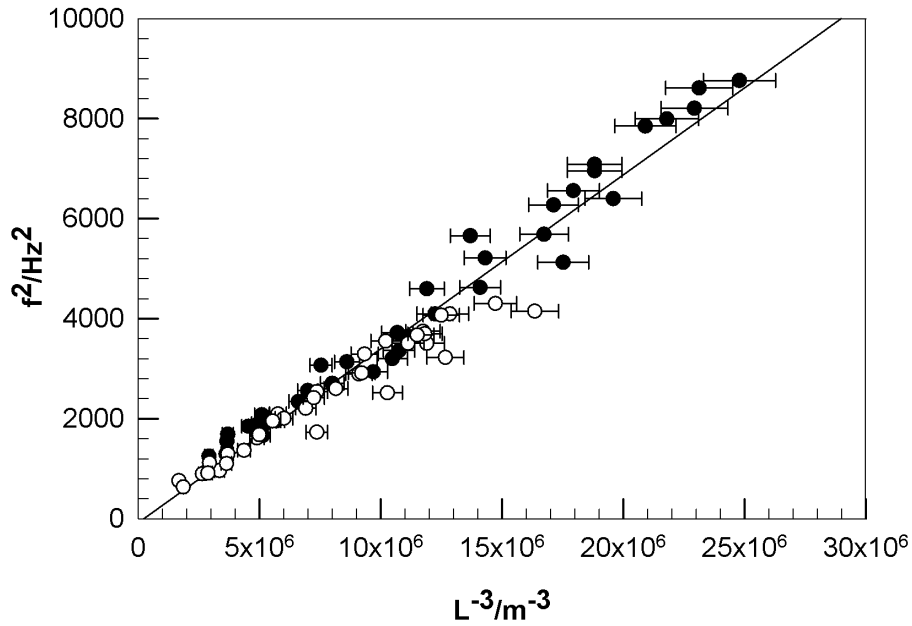er on surface of the blazed diffraction grating. For both oscillations along the long (∘) and short (•) profile lengths, the square of the frequency, f^2 is plotted as a function of L^{-3} where L is the profile length of the appropriate principle axis. The solid line shows a line of best fit through all the data. Assuming $\alpha = 0.81$, the slope of this line implies a surface tension of $\gamma = 84.2 \pm 4.0$ mNm^{-1}.*

5.2.3   Analysis of the resonant frequencies and measurement of surface tension

We now aim to investigate the positions of the two resonant peaks observed in the vibrational spectra of aspherical sessile drops which we originally predicted would correspond to standing wave states forming on the long and short profiles of the drops. Volumes of water, between 3μL and 20μL, were placed on the surface of the diffraction grating and the vibrational spectra of each drop was measured with both the major and minor axes perpendicular to the laser beam. Photographs were then taken along both axes of the drop allowing two profile lengths were measured.

Figure 5.8 shows the square of the n=2 resonant frequency peaks, f^2, plotted

out as a function of the inverse of the profile length cubed, L^{-3}. At a first glance, this plot shows a linear relationship. If we use Sharp's scaling factor, the gradient of this line implies a surface tension value of $\gamma = 84.2 \pm 4.0$ mNm^{-1} (95% confidence bounds) which is significantly higher than the literature value of $\gamma = 72.8$ mNm^{-1} [58]. Also, looking more closely shows that the datapoints corresponding to the long and short axes form lines that have different slopes. This behaviour was originally not expected as equation 2.12 indicates that, assuming α is a constant, both slopes should be the same as all the other terms in the equation have no dependence on the profile length. It can however be explained by considering α more closely which, if Noblin's approach is correct, depends on profile length/contact angle of the drop. For the elongated drops studied here, the two droplet profiles by definition must have different contact angles which is clearly visible in the photographs taken along the two principle axes of the droplets. We therefore aim to evaluate a value of α for each of the two profiles for each drop, which using Noblin's approximation where $\alpha^2 = \tanh(q\bar{h})$, involves calculating the average height of such a drop, $\bar{h}$.

In order to determine the average height of the drops, we approximated the shape of these aspherical droplets to that of an ellipsoidal cap. Although not a perfect model as the drops basal area was not perfectly elliptical, ellipses were a good match to the profiles of the drop in both the major and minor axes. Finding an analytical expression for the average height of an ellipsoidal cap is not trivial as properties of ellipses, such as the circumference, can only be evaluated using elliptical integrals. It was therefore decided that for the purposes of this study a numerical approach would need to be adopted. For every datapoint collected, ellipses were fitted to the droplet profiles (extracted from the photographs taken along the principle axes of the drop) in order to determine the characteristic dimensions of the ellipsoidal cap including the three principle radii and the offset in height between the base of the cap and centre of the ellipsoid. As with the spherical case described previously, the average height can be calculated using two methods. In both cases, contours of constant

height were defined around the surface of the ellipsoidal cap. These contours could either be used to define a volume element beneath them or a surface area enclosed between them, from which, the average height of the cap was determined. Appendix A.2 shows the details of how these two computations were performed.

Once the average height, $\bar{h}$, of each drop was known and the profile length of each axis of the drop, L_{short} and L_{long}, had been measured, α was calculated as before using the expression

$$\alpha = \sqrt{\tanh\left(\frac{n\pi\bar{h}}{L_i}\right)} \qquad (5.4)$$

where $i = long$ or $short$.

Figure 5.9 shows the result of plotting f^2 as a function of $L^{-3}\alpha^2$ where α was calculated by weighting the average height of the drop by surface area. In this plot, the two gradients that were present in Figure 5.8 are no longer obviously apparent. This is consistent with the hypothesis that oscillations along both principle axes should all fall on the same line governed by equation 2.12. Fitting a straight line to all of the data shown on the plot gives the dashed line shown in the plot, the gradient of which gives a value of surface tension to be $\gamma = 76.3 \pm 2.9$ mNm^{-1} (error calculated using 95% confidence bounds). This value is slightly higher than the literature value of $\gamma = 72.8$ mNm^{-1} [58] when the error bars are taken into account.

The gradient of the solid line shown in Figure 5.9 is the line predicted by equation 2.12 for the literature value $\gamma = 72.8$ mNm^{-1}. This appears to fit the data well, especially for larger drop sizes. The dotted line in the plot, which has a similar gradient to that of the predicted (solid) line, shows a line of best fit calculated with the 5 points at the top of the plot excluded (the 5 smallest
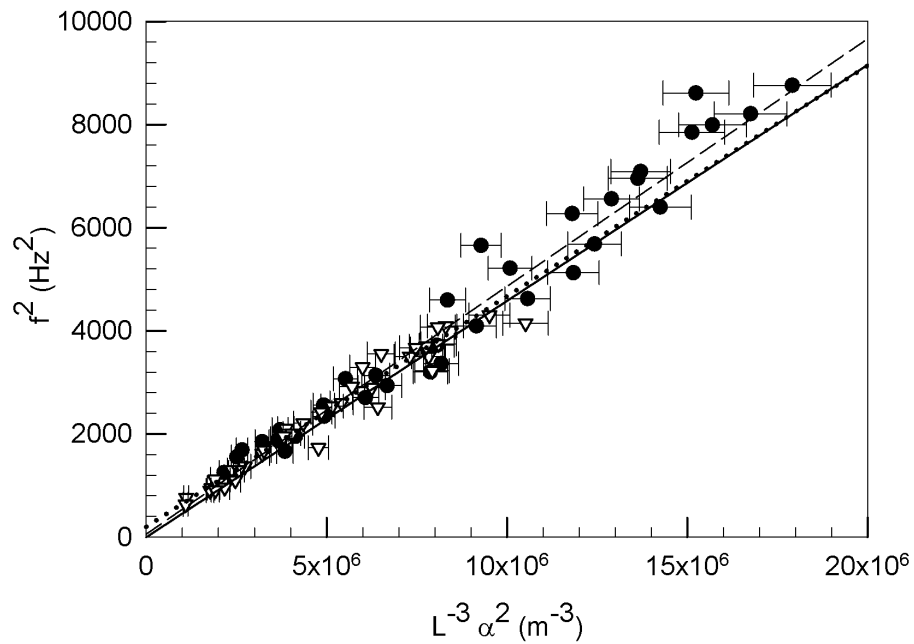
Figure 5.9: *Plot showing the position of the n=2 resonant frequency peaks in the vibrational spectra collected for aspherical droplets of water on surface of the blazed diffraction grating. For both oscillations along the long (∇) and short ($\bullet$) profile lengths, the square of the frequency, f^2 is plotted as a function of $L^{-3}\alpha^2$ where L is the profile length of the appropriate principle axis and $\alpha = \sqrt{\tanh\left(\frac{n\pi\bar{h}}{L}\right)}$. The dashed line shows a line of best fit through all the data giving $\gamma = 76.3 \pm 2.9$ mNm^{-1}. The solid line shows the line predicted by equation 2.12 for $\gamma = 72.8$ mNm^{-1} and the dotted line shows a line of best fit calculated with the 5 points at the top of the plot excluded giving $\gamma = 71.0 \pm 3.4$ mNm^{-1}.*

drops). This line has a gradient implying a surface tension of $\gamma = 71.0 \pm 3.4$ mNm^{-1} (95% confidence bounds) which is within error of the literature value. Although these five points do appear to be skewing the data, we have no real justification for excluding them - it is just an exercise to show how well the majority (around 90%) of the data fits to the literature value.

If the average height of the drop were to be weighted by volume, the two obviously different slopes corresponding to the long and short axis are also not present. A plot of this is not included because it looks essentially identical to that shown in Figure 5.9 but with a different scaling in the x-axis. The gradient of the resulting lines are significantly shallower than that of the surface area case giving for example, a value of $\gamma = 59.6 \pm 2.9$ mNm^{-1} if a straight line is fitted through all the data. We can unfortunately offer no explanation as to which is the more correct method to take. We do have to remember that the fundamental concept of modelling the drop as a liquid bath of finite depth is an approximation in itself. If we then consider the further approximation of assuming the depth of this bath is the average height of the drop, it is a testament to the model that we obtain surface tension values so close to the literature values.

The error bars shown in the plots were calculated by measuring the height of each drop in the photos taken of the two principal axes. The height of the drop in both photos should be the same and the difference in these heights was used to determine the uncertainty in distances measured from the photograph. This error was shown to be the dominant source of error in the process of measuring the profile lengths.

The results presented in this section provide substantial evidence supporting the hypothesis that the principles of Cummings's work on aspherical levitated droplets can be extended to their sessile counterparts. As predicted, the vibrational modes of the drops were shown to split into two distinct resonant

peaks. We have shown the relative amplitude of these two peaks in the measured vibrational spectra to be predominately determined by the orientation of the droplet relative to the path of the laser. When either one of the two principal axes of the drop was perpendicular to the laser beam, only one of the two frequencies was observed. The frequencies of the two resonant peaks were also shown to be governed by the same equations proposed by Noblin for the spherical case if the lower/higher frequency peak was allocated to oscillations about the long/short profile length. All of these findings support the idea that the two resonant peaks correspond to standing wave states around the two principal axes of the droplets.

In comparison to the spherical case, the contact angle dependence on α was shown to be significant. Before taking this into consideration, the gradient of the line fitted to the data implied a value of surface tension (when $\alpha = 0.81$ was used) that was higher than the literature value - this result is not possible as in the context of this experiment there is no reason why the surface tension of water can be higher than it's true value. Also, the data points relating to the long and short profile lengths did not, as implied by theory, fall onto the same line. Both of the methods presented here for calculating α were shown to resolve these issues. However, as with the spherical case, the approach of weighting the average height of the drops by volume gave values of surface tension that were significantly lower than that of the surface area calculation. When weighted by surface area, the data as shown in Figure 5.9 matches very well to that predicted by the dispersion relation using textbook values of surface tension. As a final comparison, the value of γ obtained here matches very closely to the value measured using the diamagnetic levitation technique (see Section 4.2) of $\gamma = 68.5 \pm 1.2 mNm^{-2}$. All of these factors imply that weighting the average height by surface area could be the better approach, although, we have no explanation as to why this is. However, it is worth bearing in mind that the work on spherical caps implies there could be broader issues with Noblin's approach of treating the droplets as a liquid bath of depth

$\bar{h}$ (where $\bar{h}$ is the average height of the drop). This concern stems from the fact that the theoretical values of α obtained in Section 5.1.2 by applying Noblin's model display a strong contact angle dependence that is not observed in the literature [10].

5.2.4   Analysis of damping and the estimation of viscosity

Again, if we assume bulk viscous damping, we can relate the widths of the resonant frequency peaks, ΔF, to the inverse of the profile length squared, L^{-2}. Assuming the Noblin model is correct, equation 2.14 predicts a single straight line onto which data points corresponding to oscillations along the major and minor axes should fall. The gradient of this line should give the viscosity of the liquid, η.

The widths of the n=2 resonant frequency peaks on the vibration spectra collected above were determined and plotted out in this fashion as shown in Figure 5.10. Firstly, we notice that the widths and thus the damping coefficients of oscillations about the major axis of the drop are consistently higher than that of the minor axis. The dashed lines on the plot show these two gradients. It was therefore decided that in order to gain an estimate of the viscosity we would exclude the datapoints with $L^{-2} \geq 6 \times 10^4 m^{-2}$ as the data below here is roughly linear. This is shown by the solid line which which gives $\eta = 0.89 \pm 0.06$ mPa.s (95% confidence bounds). It is also perhaps noteworthy that the gradient of this line is comparable to the slope associated with the data from the long axis of the drops. This value is a close match to the literature value of $\eta = 1.00$ mPa.s [72].

For comparison, if all of the data is included in the fit, the viscosity is calculated to be $\eta = 0.52 \pm 0.09$ mPa.s.

Figure 5.10: *Plot showing the the variation of Δf (full width at half maximum of the two resonant frequency peaks) with L^{-2} where L is the profile length of either long (∇) or short ($\bullet$) axes. In this case, the datapoints of the long and short axes do not fall onto the same line - the two dashed lines are lines of best fit through each of these sets of data. The solid line shows a line of best fit through all the data with the points above $L^{-2} = 60 \times 10^3$ excluded which were skewing the fit.*
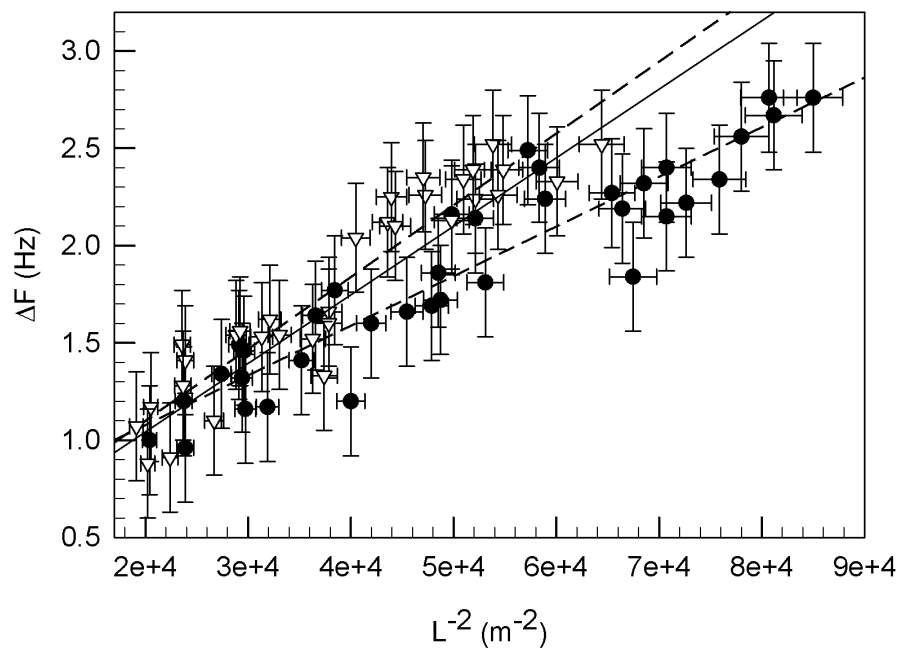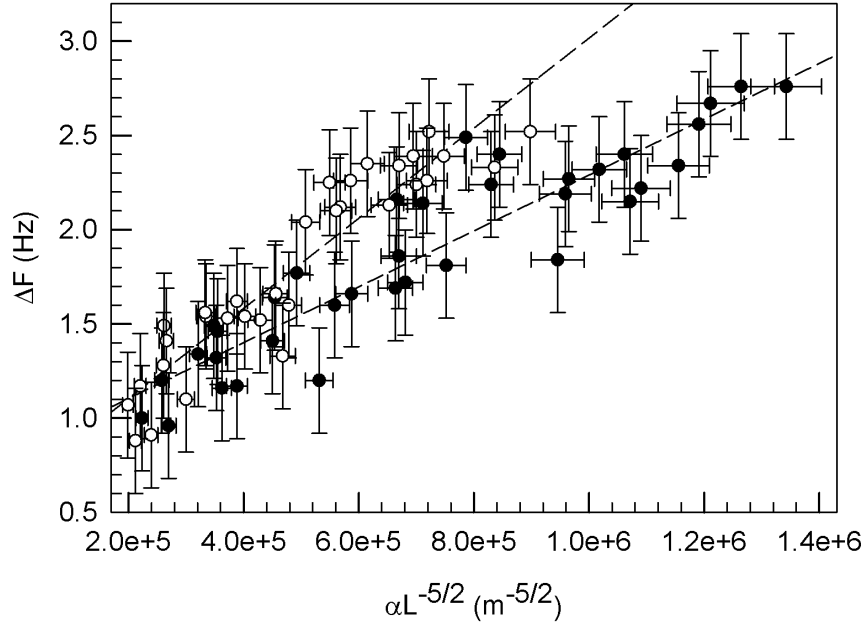
Figure 5.11: *Plot showing the the variation of Δf (full width at half maximum of the two resonant frequency peaks) with αL^{-2} where L is the profile length of either long (∇) or short ($\bullet$) axis and α is the coefficient in the dispersion relation compensating for the bath being of finite depth). This dependency is that predicted by boundary layer damping. As before, the datapoints of the long and short axes do not fall onto the same line - the two dashed lines show lines of best fit through each of these sets of data. The difference between these two gradients is greater than that when bulk viscous damping is considered (Figure 5.10).*

If we were to consider boundary layer/substrate damping rather than bulk damping, equation 2.17 implies a linear relationship between ΔF and αL^{-2}. This is plotted out in Figure 5.11 where it is can be seen that there is a greater difference between the gradients of the data corresponding to the long and short axes when compared to Figure 5.10 where bulk viscous damping was considered. This implied that, as per the work of Sharp [12], this is not the best approach to take.

In terms of testing our hypotheses, the results describing the damping of the aspherical droplets are less convincing than those described in the previous section where the position of the resonant peaks was considered. If bulk viscous damping is the dominant damping mechanism in these droplets, there is no reason from the theory presented in this thesis as to why two gradients should

be observed. The assumption that bulk viscous damping is the dominant mechanism is based not only from the work of Sharp [12] but on how well the predictions of viscosity made here match up with the values from the literature. If however interactions between the drop and the surface were significant, this could perhaps be explained by the fact that patterning of the surface would change the extent of contact line pinning and the size of the frictional iterations in the two directions. These effects would not be reflected in the equation presented for boundary layer damping (equation 2.17) as this simply considers the effects of a flat wall at the end of a bath of liquid on which capillary waves form on. Periodic patterning of the surface therefore provides a much more complex problem than that addressed by boundary layer damping. Having said this, the approach taken does allow for a reasonably accurate estimate of the viscosity of the liquid (within $\sim 10\%$ of the literature value).

Chapter 6

Vibration of Pendant Drops

When a small liquid droplet with a diameter smaller than its capillary length is suspended from the end of a pipette tip, the physics governing its shape is identical to that of small sessile drops. This chapter studies the vibrational response of pendant drops and compares them to their sessile counterparts. Noblin's model for the vibration of sessile drops treats the oscillations as standing wave states that form around the drop's profile. We aimed to determine whether this model can also be applied to pendant drops. In doing so, we also examined pendant drops with a diameter larger than the capillary length of the liquid. In this case, the shape of the drops is distorted by gravity where, if Noblin's model holds true for pendant drops, the full capillary-gravity dispersion relation needs to be considered in order to study their vibrational response.

6.1   Experimental details

As described in Section 3.2, the same techniques used for the experiments on sessile drops was used to perturb and measure the vibrational response of pen-
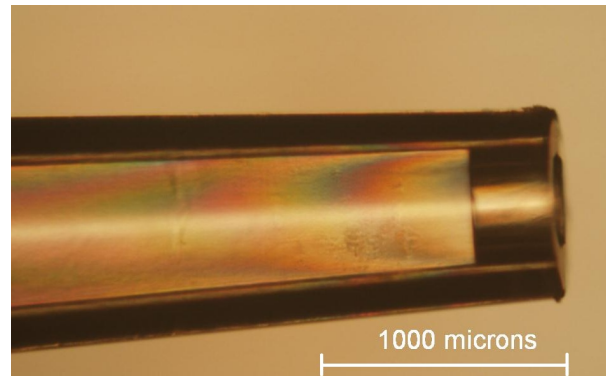
Figure 6.1: *Optical micrograph of one of the pipette tips used. The tip has an outer diameter 0.77mm and inner diameter 0.37mm at the end.*

dant water droplets. These drops were suspended from the end of a pipette tip (Scientific Laboratory Supplies, PIP9044) using 0.5mL polypropylene syringes (Becton Dickinson). An optical micrograph of one of these pipette tips is shown in Figure 6.1. As before, the impulse used was a puff of nitrogen gas and the oscillations in the laser light scattered off the drop were detected using a photodiode. The signal from which was amplified, sampled at a frequency of 1000Hz using the data acquisition card (National Instruments USB-6008) and Fourier transformed giving the vibrational spectra from which the position and width of the resonant frequency peaks could be extracted. Once this data was collected, photographs of each drop were collected using a MantaG125B camera (Allided Vision Technologies). These images were used to extract the profiles of the droplets.

An example set of data for a pendant drop is included in Figure 6.2 where plots of the the photodiode signal and the vibrational spectrum are shown. This droplet had a resonant frequency of 37.6 ± 0.2 Hz forming a peak in the spectra with a full width at half maximum of 0.9 ± 0.28 Hz. The photograph of the drop and a plot of the extracted profile are also included in the figure, from which the profile length was calculated to be 4.3 ± 0.1 mm. The time dependent data and its Fourier transformation are very similar to that collected for a comparable spherical sessile drop - Figure 5.1 (in Section 5.1.1) shows the vibrational spectra of a sessile drop with a profile length of 6.1 ± 0.1 mm.
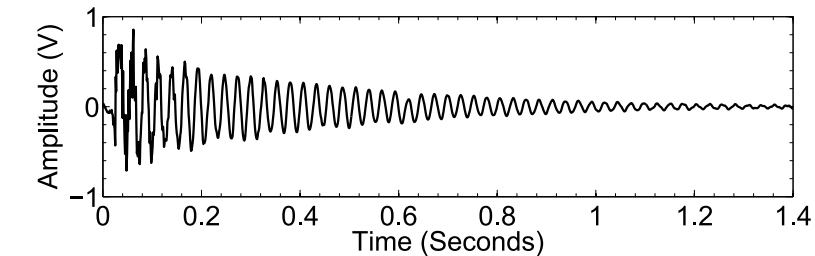
(a) *Photodiode Signal*
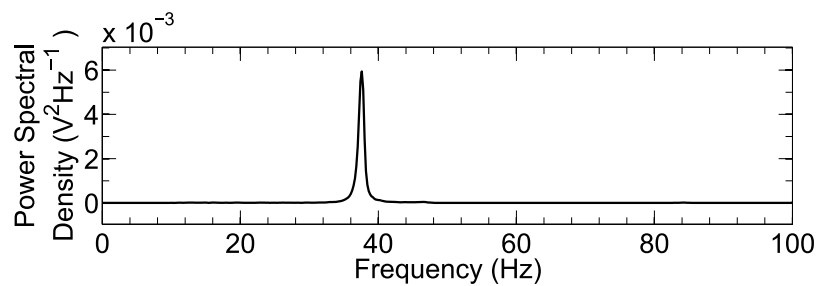
(b) *Vibrational Spectra*
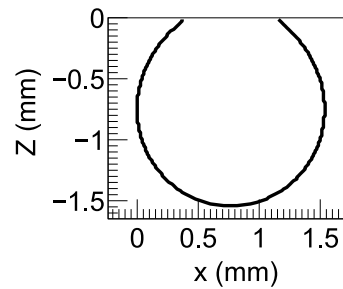
(c) *Photograph of Drop*   (d) *Drop Profile*

Figure 6.2: *Example set of data for a water droplet of profile length $L = 4.3mm$ suspended from the end of a micropipette tip. (a) shows the time dependent voltage fluctuations collected from the photodiode which was fourier transformed to give the vibrational spectra in (b). The peak shown, corresponding to the n=2 mode, is at 37.6Hz with a full width at half maximum of 0.9Hz. The photograph of the droplet (c) was used to extract the profile of the drop shown in (d).*

6.2 Analysis of the resonant frequencies

Vibrational spectra were collected for pendant drops with profile lengths ranging from $L = 1.8$ mm to $L = 9.8$ mm which was the largest range of drops possible for the pipette tip used (the end of which had a diameter of 0.77mm). A selection of these drops are pictured in Figure 2.8 (Section 2.4). The position of the fundamental resonant peak, f, was plotted as a function of L^{-3} as per equation 2.12 which was derived from the capillary term of the dispersion relation for capillary-gravity waves on a liquid bath of finite depth (equation 2.11). This is shown in Figure 6.3 where the data behaves as predicted by the the dispersion relation. For small drops, in the capillary regime, the data forms a straight line but as the drop size increases (moving from the right side to left side of plot), the data curves towards the origin. The solid line in Figure 6.3 shows a straight line fitted to this linear region ($L^{-3} \gtrsim 3 \times 10^{8} m^{-3}$). Assuming these fundamental peaks represent n=2 oscillations, that the density of water is $\rho = 998 kgm^{-3}$ [57] and that $\alpha = 0.81$(Sharp's scaling factor [10]), equation 2.12 gives the surface tension of the water to be $\gamma = 60.2 \pm 2.6$ mNm^{-1} (95% confidence bounds) from the gradient of the line.

This value for surface tension is consistent with the result obtained using the Wilhelmy plate technique (see Section 4.1) where $\gamma \approx 60$ mNm^{-1} was measured for deionised water from the same ELGA purification unit. It is a bit lower than that obtained using the magnetic levitation technique $\gamma = 68.5 \pm 1.2$ mNm^{-1} but as discussed in Chapter 4, it is suspected this is due to the fact the levitation experiments were conducted in an enclosure isolating the experiment from ambient conditions. The pendant drop experiments, Wilhelmy plate technique etc. also a much less clean system when compared to the levitation experiment as the water come into contact with more surfaces from which it is possible to pick up contaminates.

Figure 6.4 shows the dependency of the frequency f with the wavenumber $q =$
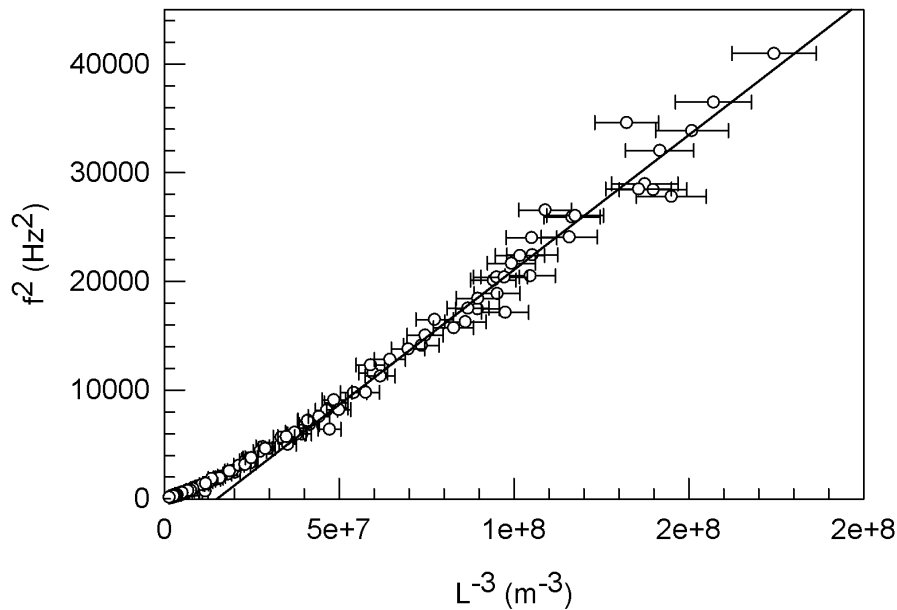
Figure 6.3: *Plot of the n=2 modes for pendant drops of water suspended from the end of a pipette tip. The square of the frequencies are plotted against L^{-3} where L is the profile length of the drop. The solid line passes through the regime where the drops have diameter smaller than the capillary length. Using equation 2.12, this line corresponds to a surface tension of $\gamma = 60.2 \pm 1.3$ mNm^{-1} assuming $\alpha = 0.81$.*

Figure 6.4: *A plot of the resonant frequency, f, against the wavenumber, $q = 2\pi/\lambda$ for pendant water droplets. The two gradients shown in the figure represent the power law dependency of the gravity ($q < 1000$) and capillary ($q > 1000$) regimes. The power laws predicted by the dispersion relation are 1 and 1.5.*

$2\pi/\lambda$ on a log-log plot. This plot can be compared directly to that of Noblin who did the same thing for sessile drops [50]. Here the transition from ca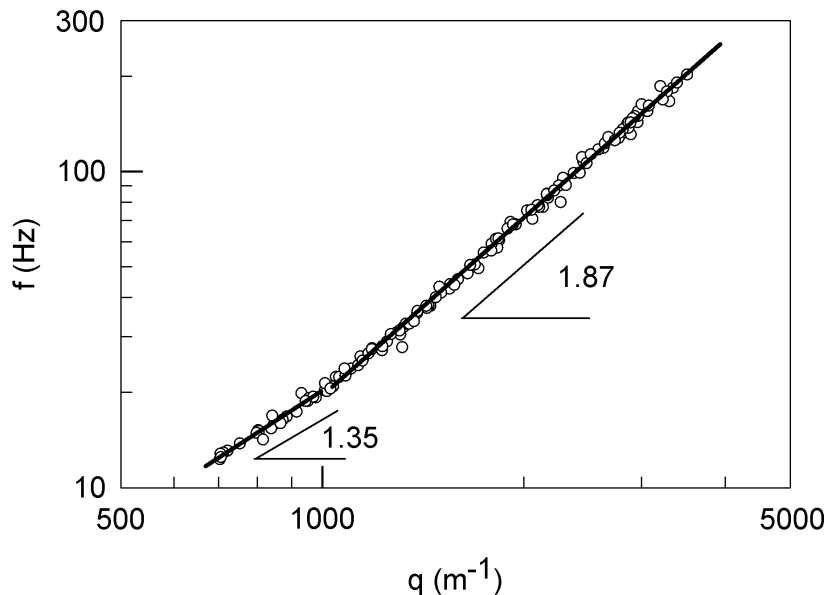pillary to gravity regimes is at $q \approx 1000 m^{-1}$. Applying simple laws of logarithms to the dispersion relation for capillary-gravity waves (equation 2.11) allows us to predict the gradients in these two regimes to be 1.5 and 1 respectively (representing the power laws in the dispersion relation). Fitting straight lines to these two regions, gives gradients of 1.87 ± 0.01 and 1.35 ± 0.05 for the capillary and gravity regimes respectively. Although these two gradients do not perfectly match the theoretical values predicted by equation 2.11, the difference between the two gradients matches (within error) the difference between the theoretical values.

At the transition point between the two regimes, we would expect the drops to have a diameter that is comparable to the lengthscale described by the capillary length, l_c. Since $\gamma \approx 60$ mNm^{-1} (calculated above), we can use our equation for the capillary length (equation 2.4) to give $l_c \sim 2.5$mm. From taking measurements of photographs/droplet profiles corresponding to $q \approx 1000$ m^{-1}, the droplets at the transition point between the capillary and gravity regimes 6.4 have a diameter $D \approx 2$mm . As equation 2.4 only gives an indication of lengthscale of the crossover point rather than a precise value, these results would appear to be consistent. Finally, if we look back to Figure 2.8, we can see that, at this length-scale, the drops have started to become obviously deformed due to the influence of gravity. This adds further credibility to the significance of the $q \approx 1000$ m^{-1} transition point on Figure 6.4.

6.3 Analysis of damping

Secondly, we consider the damping of these oscillations. Again, as the physics of small pendant drops should be identical to that of small sessile drops, we can therefore apply the work of Sharp [10] and assume the dominant damping
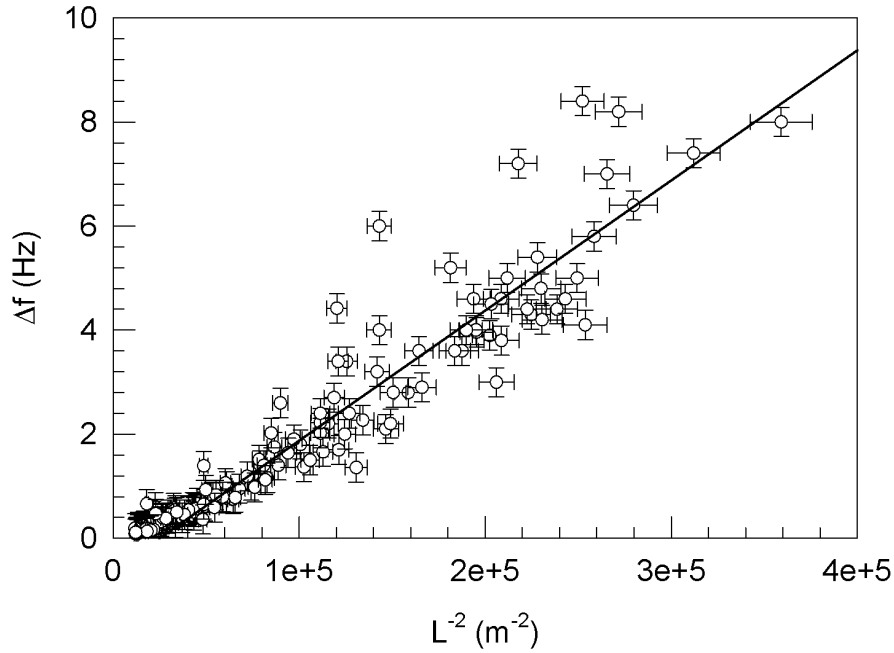
Figure 6.5: *A plot showing the dependence of the full width at half maximum Δf of the resonant frequency peaks with L^{-2} where L is the profile length. From the gradient of the line shown (which is a line of best fit excluding the points below $L^{-2} = 0.5 \times 10^5 \ m^{-2}$) the viscosity of the liquid was calculated to be $\eta = 0.63 \pm 0.32$ mPa.s.*

mechanism is that of bulk viscous damping. Figure 6.5 shows how the full width at half maximum Δf varies with L^{-2} where there is a clear linear dependence despite the large amount of scatter in data. If a line is fitted through the capillary regime (i.e. excluding the curvature below $L^{-2} = 0.5 \times 10^5$ m^{-2}) and the gradient extracted, equation 2.14 gives us $\eta = 0.63 \pm 0.32$ mPa.s. Although this value is lower than both the literature value of $\eta = 1.00$ mPa.s [72] and those obtained in Chapter 5, the scatter has resulted in a very large error of $\sim 50\%$. Taking this into account, even though the literature value is almost within error, it is hard to draw any meaningful conclusion from this data.

Chapter 7

Summary and Discussion of Key Results

The previous chapters, through studies of the resonant frequencies and damping coefficients of oscillations in sessile drops, have stated a number of values for the surface tension and viscosity of water. Here we bring all of these results together for comparison.

7.1 Surface tension

The various values of surface tension obtained from both the spherical and aspherical cases are included in table 7.1 along with the measurements taken in Chapter 4, using the Wilhemy plate and levitated methods. For reference, the literature value is $\gamma = 72.8$ mNm^{-1} [58].

Unfortunately, there is a wide range of values given here and we are unable to present explanations as to why they are all so different. However, a good starting point is to consider the values obtained for the Wilhelmy plate and

Table 7.1: *A summary of the key measurements of surface tension, γ, obtained in this chapter using the different values of α determined. All errors calculated apart from those of Wilhelmy plate results calculated from 95% confidence bounds. Some notes on the values obtained:*
• *indicates this value is an estimate from observations and does not represent a set of repeatable measurments.*
* *indicates value is an average across all of the values of α calculated for the short/long axis.*
† *offers an alternative result with 5 points of data excluded from the fit corresponding to the smallest droplets.*

Method	α method	α value	γ (mNm^{-1})
Wilhelmy Plate ($\sim$10min) (Section 4.1)	N/A	N/A	60 ± 3
Wilhelmy Plate ($\sim$1min) (Section 4.1)	N/A	N/A	$70 \pm 5^{\bullet}$
Levitation (Section 4.2)	N/A	N/A	68.5 ± 1.2
Spherical Sessile Drop (Section 5.1)	Sharp	0.81	65.5 ± 1.0
	$\bar{h}$ by area	0.89	54.1 ± 1.0
	$\bar{h}$ by volume	0.97	45.7 ± 1.0
Aspherical Sessile Drop (Section 5.2)	Sharp	0.81	84.2 ± 4.0
	$\bar{h}$ by area	0.85/0.81*	$76.3 \pm 2.9, 71.0 \pm 3.4^{\dagger}$
	$\bar{h}$ by volume	0.96/0.94*	59.6 ± 2.9
Pendant Drop (Chapter 6)	Sharp	0.81	60.2 ± 2.6

levitation methods. As discussed in Chapter 4, these results are consistent with the observations of Henderson and Miles [70] who observed contamination to start taking an effect on surface tension measurements after 1 minute of the liquid being exposed. The value stated for measurements after ~ 1 minute is an estimate based on observations mentioned in Section 4.1. It is suspected a reason why the levitated result is of a magnitude expected for an uncontaminated sample is because the measurements were essentially taken in a closed box minimising contamination from the surrounding air. This is again consistent with the findings of Henderson and Miles [70]. The levitation technique is also inherently cleaner as the liquids come into contact with less surfaces.

We now compare these values to the sessile drop experiments. Firstly, it is worth noting that these experiments were conducted on the time-scales of approximately 1 minute so we would expect, based on the data just discussed, to obtain a value in the region between 65 mNm^{-1} and the literature value of $\gamma = 72.8$ mNm^{-1} [58]. The result obtained using Sharp's scaling factor [10] for the spherical cap experiment, $\gamma = 65.5 \pm 1.0$ mNm^{-1}, just falls at the lower end of this regime. This is not surprising, as although care was taken when preparing the PDMS substrate used in this experiment, the substrate was not new when the experiments were performed. This means that contaminants from the atmosphere may also be present on the surface. It is also worth noting that there is a possibility that residual cross-linking agent or monomer may be present which could potentially also cause contamination of the drop.

Unfortunately, the surface tension values for spherical drops obtained using our calculated values of α are too small to make physical sense when considering the results discussed above. As discussed in Section 5.1, this could imply the model, which assumes the oscillations are capillary waves on a liquid bath of depth $\bar{h}$ ($\bar{h}$ is the average height of the drop), is too much of an approximation to make measurements of the accuracy we would like. It could equally imply

that the calculations presented in Appendix A.1 are not correct. As discussed in Section 5.1, the value of α corresponding to Sharp's scaling factor could be the most appropriate approach to take. This is because it was calculated experimentally and therefore does not rely on approximating the height of the bath.

The results for the aspherical drops add another complication to this story. Firstly, having concluded that Sharp's scaling factor might be the most appropriate value of α to use for the spherical case, we can say with certainty this is not the case for aspherical droplets. Firstly, the surface tension value it implies for water is so large it is non-physical. Secondly, as shown in Figure 5.8, the datapoints corresponding to oscillations around the long and short axes do not fall onto the same line. By calculating α, numerically as described in Appendix A.2, we remove the issue of the datapoints not collapsing onto a single line and bring the surface tension values down to a magnitude where they are not impossibly high. For the case where the average height is weighted by volume, the value of γ, as in the spherical case, seems too low. However, the surface tension value calculated from weighting the average height of the drop by surface area gives a value very close to the literature value (only just outside the error bar).

It is also shown here that by excluding the 5 smallest droplets from the fit used gives $\gamma = 71.0 \pm 3.4$ mNm^{-1} which is within error of the literature value. Although we have no reason for excluding these datapoints from the fit, what it does show is that the literature value is a close match to 67 out of 75 (about 90%) of the datapoints on the plot. If we now compare this value to the values of surface tension collected in the Wilhelmy plate, levitation and spherical cap experiments, at a first glance it is too large. However, when taking the aspherical data, greater care was taken over making sure everything was clean as to minimise any contamination issues when compared to the other experiments. Considering this and the fact the data was also collected quickly

($\sim$ 1 minute), we would expect this experiment to give us a relatively high value for the surface tension. Although it is tempting to conclude from this that weighting the average height is the correct approach, the fact it gives the "correct" answer is not an acceptable justification. This is especially true when this approach gives such a questionable result in the spherical cap case.

The final result to consider is that of the pendant drop experiment. Using Sharp's scaling factor we get the result of $\gamma = 60.2 \pm 2.6$ mNm^{-1}. It is worth noting here that the droplets used were exposed to ambient conditions for over 5 minutes. This is therefore consistent with the findings of the Wilhelmy plate experiments.

It is also worth noting that the sessile experiments were conducted using LCMS grade deionised water (Sigma-Aldrich) which, in theory, should contain fewer contaminants than the deionised water from the ELGA purification system used for the Wilhelmy and levitation and pendant experiments. However, it is predicted that the differences in the resulting surface tensions will be minimal when considering the other factors discussed.

7.2 Viscosity

For spherical sessile drops, aspherical sessile drops and pendant drops, values of viscosity were calculated by assuming bulk viscous damping was the dominant damping mechanism. The results are included in table 7.2. If all the data from the plots is included in the calculations, all the values are around a factor of 2 too small when compared to the literature value of $\eta = 1.00$ mPa.s [72]. This factor of 2 was also reported by Sharp [12]. In the case of sessile drops, if just the linear regions on the plots of Δf against L^{-2} were used in the calculations (by excluding data corresponding to the smallest drop sizes), the results are within around 10% of the literature value.

Table 7.2: *Comparison of the viscosity values. In the cases of sessile drops, the results shown in brackets are from calculations where small drops were excluded from the calculations so that only the linear region of the plots were included. 95% confidence bounds were used to calculate the errors.*

Method	Viscosity (mPa.s)
Spherical Sessile Drop (Section 5.1)	0.52 ± 0.11 (0.88 ± 0.04)
Aspherical Sessile Drop (Section 5.2)	0.52 ± 0.09 (0.89 ± 0.06)
Pendant Drop (Chapter 6)	0.63 ± 0.32

Chapter 8

Conclusions

This thesis presented several experiments used to analyse the vibrational response of sessile and pendant droplets. The technique used was a simple optical deflection technique in which laser light was scattered off the droplets onto a photodiode. When perturbed using a short puff of nitrogen gas, the droplets oscillated at their resonant frequencies. The time dependent intensity fluctuations measured by the photodiode were Fourier transformed giving the vibrational spectra of the droplets. From this spectra, the position and width of the n=2 fundamental resonant peaks were extracted. The width (full width at half maximum) is equivalent to the damping coefficient of the oscillations [12]. For each droplet measured, the profile lengths of the droplets were measured from photographs taken of the droplet profiles.

A simple theory of droplet vibration, proposed by Noblin [50], was used to analyse these oscillations. This theory treats these oscillations as standing standing capillary wave states forming around the profile of the drops. The surface of the drops were modelled as a liquid bath of finite depth with a length equal to the profile length of the drop. This allowed the oscillations to be described by the dispersion relation for capillary-gravity waves which

was used to relate the frequency of oscillations to the profile length of the droplets. This dependence allowed the surface tension of the drops to be measured. The viscosity of the liquid was also measured by considering the relationship between the damping coefficient (assuming bulk viscous damping) of the oscillations and the profile length of the drops [12].

The vibrational spectra of small (diameter smaller than the capillary length) spherical cap drops and pendant drops were both analysed using these methods. The values for surface tension extracted were consistent with measurements taken using well established techniques (oscillations in levitated droplets and the Wilhelmy plate technique) when the degree of likely contamination of the droplet was taken into consideration. The gravity dominated regime was also investigated in the case of pendant drops and compared to Noblin's analysis of sessile drops. The two were shown to behave similarly. We also explored the α coefficient in the dispersion relation and, for the case of spherical caps, derived using two methods showing the how α depends on the contact angle. Neither of these methods showed results that were consistent with values determined experimentally from the literature [10].

The anisotropic wetting properties of surfaces patterned with periodic groves were utilised to produce droplets with an aspherical geometry. The vibrational response of these drops was studied using the same optical deflection technique. It was originally predicted that, based on the theory of aspherical levitated drops [66], that the vibrational spectra of aspherical sessile drops would show two closely spaced peaks corresponding to oscillations around the major and minor axes of the drop. We showed this was in fact the case. We also showed that Noblin's model could be extended to describe these oscillations. The resonant peaks corresponding to oscillations around both the long and short axes were shown to obey the same dispersion relation. When plotted out, the two sets of peaks collapsed onto the same line of constant surface tension. Depending on the approach taken in accounting for the depth of the liquid

bath that features in Noblin's model, the surface tension was measured to be within error of the literature value of $\gamma = 72.8$ mNm^{-1} [58].

Measurements of viscosity, assuming bulk viscous damping was the dominant damping mechanism, were also taken for the three types of drop. All three provide values within the factor of two of the literature value of $\eta = 1.00$ mPa.s [72].

Chapter 9

Future Work

There are many directions in which this study could be taken; a small section of which are outlined in this chapter. Firstly, the most obvious extension of this study would be to study different liquids. This has been difficult previously as low surface tension liquids have a tendency to wet to most surfaces so producing sessile/pendant droplets using them was a challenge. However, when placed on the substrates made using the methods outlined in Appendix B, certain low surface tension liquids, such as hexadecane, bead up into droplets with contact angles greater than 100°. We have also shown that glass capillaries can be coated in the same way so low surface tension measurements of pendant drops should also be possible without the liquid wetting to the side of the tube. Being able to make measurements of liquids of a range of different surface tensions would be beneficial in demonstrating the potential application of this technique for measuring surface tension and viscosity.

In relation to the work on aspherical droplets, the techniques used here have the potential to to applied to the investigation of phenomenon such droplet pinning, contact angle hysteresis and anisotropic wetting properties. A simple example of the latter is how liquids evaporate from such patterned surfaces.

Droplets of more complex fluids, such as colloidal solutions could also be examined using the techniques presented here. The effects of introducing molecules that stay at the liquid/air interface whilst not affecting the bulk properties could also be of interest in understanding, for example, the effects surface contaminants have on the damping of droplet oscillations.

The technique could be applied is in measuring the surface tension and viscosity of ionic liquids in ultra high vacuum. Traditional methods for measuring the surface tension and viscosity would be extremely difficult to conduct under vacuum and the concept of using droplet oscillation could be an attractive one to scientists working in this area.

Another simple experiment would be to use the Wilhelmy plate technique to investigate more conclusively how the surface tension of liquids vary with time as a result of contamination. This could provide more conclusive evidence to support the some of the discussion presented in this thesis.

The oscillating droplet technique also has the potential to be used to determine rheological properties of viscoelastic materials. We have conducted preliminary work using solutions of poly(acrylamide-co-acrylic acid) dissolved in water. These solutions have a very obvious viscoelastic properties, and when their resonant properties are studied using the levitation technique described in Section 3.3, the elastic component appears to be detectable in the frequencies measured. Data collected for the l=2 mode shows that increasing the concentration and thus the size of the elastic response of the liquid increases frequencies measured - this is the expected result as the elastic component acts as an additional restoring force. Theoretical studies have been conducted in which the frequency response of viscoelastic spherical drops are predicted [73]. If the rheological properties, such as Deborah and Reynolds numbers, of these poly(acrylamide-co-acrylic acid) solutions were known we would be able to compare the our data with those predicted by this theory. These values can

be experimentally determined given access to an appropriate rheometer.

We would like to take the investigation of viscoelastic properties of drops further and see if rheological properties can be measured using the vibration of sessile drops. We have shown that it is possible to excite the vibrational modes of Poly(acrylamide-co-acrylic acid) sessile droplets. However, we have not had the time to pursue it further. If a sufficient understanding of levitated viscoelastic drops is gained, applying the ideas to the sessile case could result in a cheap and simple method for determining the rheological properties of viscoelastic liquids.

Appendix A

Average Height of a Sessile Droplet

A.1 Spherical cap

A.1.1 Average height weighted by volume

The problem is set out in Figure A.1 for a spherical cap of radius, R with a contact angle, θ to the surface.

Firstly, we find the total volume of the spherical cap. We define the volume, V, to be the sum of tube like volume elements, of volume dV, defined from contours of constant height around the surface of the drop. From the diagram we can see that

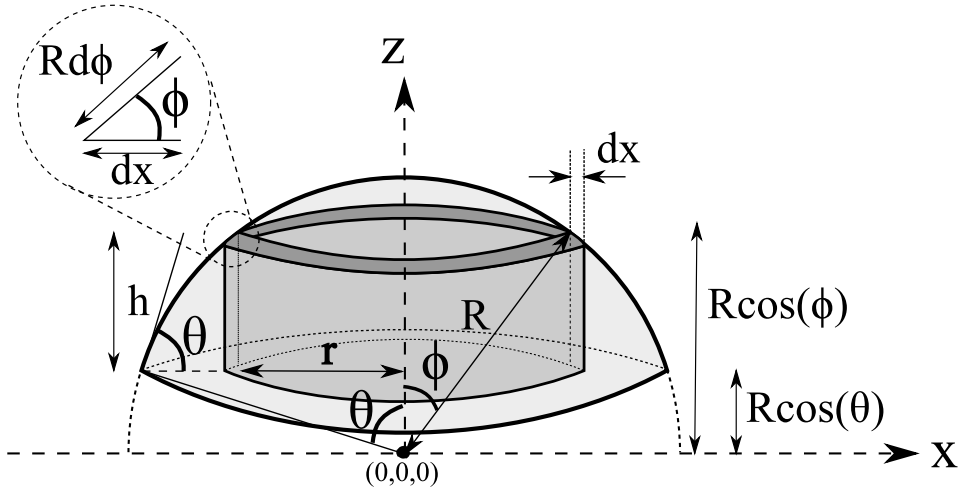$$dV = h(2\pi r)(R cos\phi d\phi) \tag{A.1}$$

Figure A.1: *Geometry of a spherical cap*

Substituting in expressions for the radius, $r = R \sin \phi$, and height of the tube, $h = R \cos \phi - R \cos \theta$, we have

$$dV = 2\pi R^3 \left(sin\phi \cos^2 \phi - \sin \phi \cos \phi \cos \theta \right) d\phi \tag{A.2}$$

This can be solved for V by integrating between between $\phi = 0$ and $\phi = \theta$

$$V = \int_{\phi=0}^{\phi=\theta} dV \tag{A.3}$$

$$= 2\pi R^3 \int_0^\theta \left(\sin \phi \cos^2 \phi - \sin \phi \cos \phi \cos \theta \right) d\phi \tag{A.4}$$

$$= 2\pi R^3 \left[-\frac{\cos^3 \phi}{3} + \frac{\cos^2 \phi \cos \theta}{2} \right]_{\phi=0}^{\phi=\theta} \tag{A.5}$$

which gives the total volume of the cap to be

$$V = \frac{\pi R^3}{3} \left(\cos^3 \theta - 3 \cos \theta + 2 \right) \tag{A.6}$$

The mean height of the cap was evaluated by defining $\frac{dV}{V}$ as a probability distribution that describes how much volume there is under the surface of the drop at points of height h. The mean height is therefore by definition

$$\bar{h} = \sum_i \frac{dV_i}{V} h_i \tag{A.7}$$

For a continuous distribution this becomes

$$\bar{h} = \frac{1}{V} \int_a^b h dV \tag{A.8}$$

which can be solved by substituting in the expression for dV (Equation A.1) giving:

$$\bar{h} = \frac{1}{V} \int_{\phi=0}^{\theta} h(2\pi R^2 h \sin\phi \cos\phi d\phi) \tag{A.9}$$

$$= \frac{2\pi R^4}{V} \int_{\phi=0}^{\theta} (cos\phi - \cos\theta)^2 \sin\phi \cos\phi d\phi \tag{A.10}$$

$$= \frac{2\pi R^4}{V} \left[-\frac{\cos^4\phi}{4} + \frac{2\cos^3\phi\cos\theta}{3} - \frac{cos^2\phi\cos^2\theta}{2} \right]_{\phi=0}^{\phi=\theta} \tag{A.11}$$

Substitution of the equation for the total volume, V (Equation A.6), and some simple algebra gives us the following expression for the average height of a spherical cap weighted by the volume of liquid under the contours of constant height.

$$\bar{h} = \frac{R}{2} \left(\frac{-\cos^4\theta + 6\cos^2\theta - 8\cos\theta + 3}{\cos^3\theta - 3\cos\theta + 2} \right) \tag{A.12}$$

For a circle, the ratio of an arc and a circumference is equal to the ratio of the radian measure of that arc and 2π. This gives us the relationship between the profile length of the spherical cap and the contact angle:

$$\frac{L}{2\pi R} = \frac{2\theta}{2\pi} \tag{A.13}$$

$$L = 2R\theta \tag{A.14}$$

Since $\alpha = \sqrt{\tanh(q\bar{h})}$ and the wavenumber, $q = \frac{2\pi}{\lambda} = \frac{n\pi}{L} = \frac{n\pi}{2R\theta}$, we get

$$\alpha = \sqrt{\tanh\left(\left(\frac{n\pi}{4\theta}\right)\frac{-\cos^4\theta + 6\cos^2\theta - 8\cos\theta + 3}{\cos^3\theta - 3\cos\theta + 2}\right)} \tag{A.15}$$

A.1.2   Average height weighted by surface area

The average height weighted by the surface area can be calculated using a similar method to that described above. Contours of constant height were again used, this time to split the surface into rings with surface area element

$$dA = (2\pi r)(Rd\phi) \tag{A.16}$$

$$= 2\pi R^2 \sin\phi d\phi \tag{A.17}$$

so that the total area, A is given by

$$A = \int_{\phi=0}^{\theta} dA \tag{A.18}$$

$$= 2\pi R^2 \int_{\phi=0}^{\theta} \sin\phi d\phi \tag{A.19}$$

$$= 2\pi R^2 \left(1 - \cos\theta\right) \tag{A.20}$$

The average height is defined using an equivalent probability distribution

$$\bar{h} = \sum_i \frac{dA_i}{A} h_i \tag{A.21}$$

which, for a continuous distribution becomes

$$\bar{h} = \frac{1}{A} \int_a^b h dA \tag{A.22}$$

Using equations A.17 and A.20 this can be solved:

$$\bar{h} = \frac{1}{2\pi R^2 (1 - \cos\theta)} \int_{\phi=0}^{\theta} \Big((R\cos\phi - R\cos\theta)(2\pi R^2 \sin\phi d\phi) \Big) d\phi \tag{A.23}$$

$$= \frac{R}{1 - \cos\theta} \int_{\phi=0}^{\theta} \left(\sin\phi\cos\phi - \sin\phi\cos\theta\right) d\phi \tag{A.24}$$

$$= \frac{R}{1 - \cos\theta} \left[\frac{\sin^2\phi}{2} + \cos\phi\cos\theta \right]_{\phi=0}^{\phi=\theta} \tag{A.25}$$

$$= \frac{R}{2(1 - \cos\theta)} \left(\cos^2\theta - 2\cos\theta + 1\right) \tag{A.26}$$

As before,

$$\alpha = \sqrt{\tanh(q\bar{h})} \tag{A.27}$$

$$= \sqrt{\tanh\left(\frac{n\pi}{4\theta}\left(\frac{\cos^2\theta - 2\cos\theta + 1}{1 - cos\theta}\right)\right)} \tag{A.28}$$

A.2   Ellipsoidal cap

The approach taken here is a variation on the methods used for spherical caps previously (Appendix A.1). However, because of the nature of ellipses, the problem becomes a lot more complex to solve analytically. This is due to the requirement to solve elliptical integrals in order to determine properties like the circumference. A numerical approach was therefore taken making use of the functions built into Matlab (Mathworks) designed to solve these integrals.

In order to calculate $\bar{h}$ and thus α for the datapoints collected, ellipses were fitted to the droplet profiles that had already been extracted (see section 3.1). This was done using another Matlab script based around a least squares method where initial values were given using a GUI (see Figure A.2a). The dimensions extracted were the elliptic radii - a, b, and c - in the major (x), minor (y) and vertical (z) axis respectively, the basal radius of the drop along the major axis, r_x, and the z-offset between the origin of ellipse and the base of the drop, y_0. These quantities are defined in Figure A.2b. The parameters of the two ellipses calculated for each drop were used to characterise an ellipsoidal cap that is a best approximation to the shape of the drop.
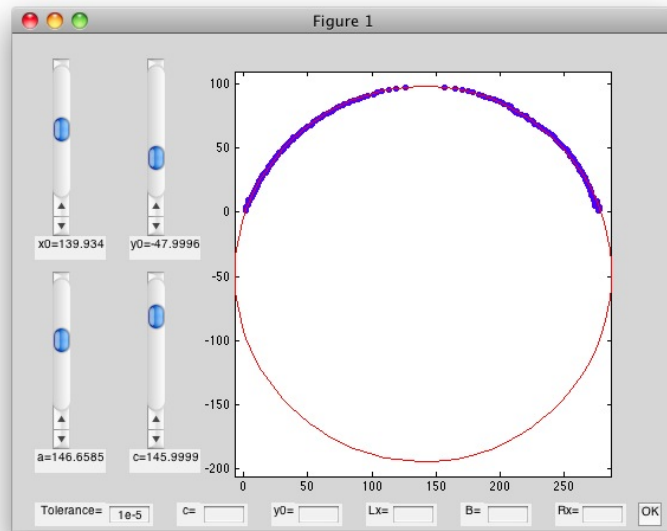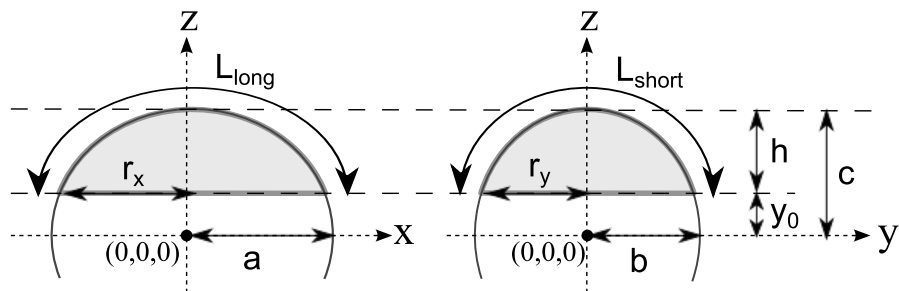
(a) *Ellipse fitting software GUI*

(b) *Geometry of an ellipsoidal cap*

Figure A.2: *(a) The GUI designed in Matlab used to fit ellipses to droplet profiles (extracted as described in section 3.1).   (b) The geometry of the long and short axis of an ellipsoidal cap (shaded region) at a height y_0 from the origin*

A.2.1   Average height weighted by volume

A similar method to that described in Appendix A.1.1 was used where the ellipsoidal cap is divided into tube-like volume elements. For N iterations of x values between $x = 0$ and $x = r_x$, the following calculations were computed to work out the volume element at a point (x,y,z).

Taking the ellipse forming the profile of the long axis, the value of z at position x was calculated from the equation of an ellipse in the x-z plane:

$$1 = \frac{x^2}{a^2} + \frac{z^2}{c^2} \tag{A.29}$$

$$z = c\sqrt{1 - \left(\frac{x^2}{a^2}\right)} \tag{A.30}$$

The height of the drop at point z is therefore

$$h = z - y_0 \tag{A.31}$$

If we take the plane passing through the drop at height h that is perpendicular to the z axis, we can calculate the two elliptic radii of the elliptical cross section in that plane. R_x is simply the value of x and R_y can be calculated using the equation of the ellipse in that plane.

$$R_x = x \qquad\qquad R_y = b\sqrt{1 - \left(\frac{z^2}{c^2}\right)} \tag{A.32}$$

The eccentricity, ε, can then be calculated using the expression

$$\varepsilon = \sqrt{1 - \frac{R_y}{R_x}} \tag{A.33}$$

allowing the complete elliptical integral of the second kind, $E(\varepsilon)$, to be evaluated using the Matlab function *ellipke*. The circumference at height z, C, can then be calculated:

$$C = 4R_x E(\varepsilon) \tag{A.34}$$

The volume element is then simply

$$dV = Chdx \tag{A.35}$$

Once this has been done for all N iterations, the volume and average height can be calculated:

$$V = \sum_{i=1}^{N} dV_i \tag{A.36}$$

$$\bar{h} = \frac{1}{V} \sum_{i=1}^{N} h_i dV_i \tag{A.37}$$

A.2.2   Average height weighted by surface area

The approach taken here is more complex than the other calculations in this appendix. The surface of the ellipsoid is split up into rings, but calculating
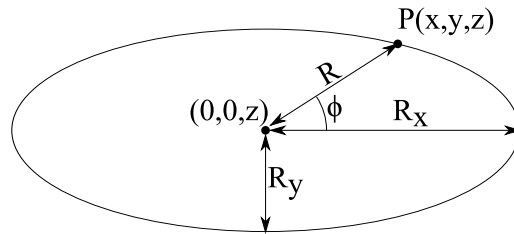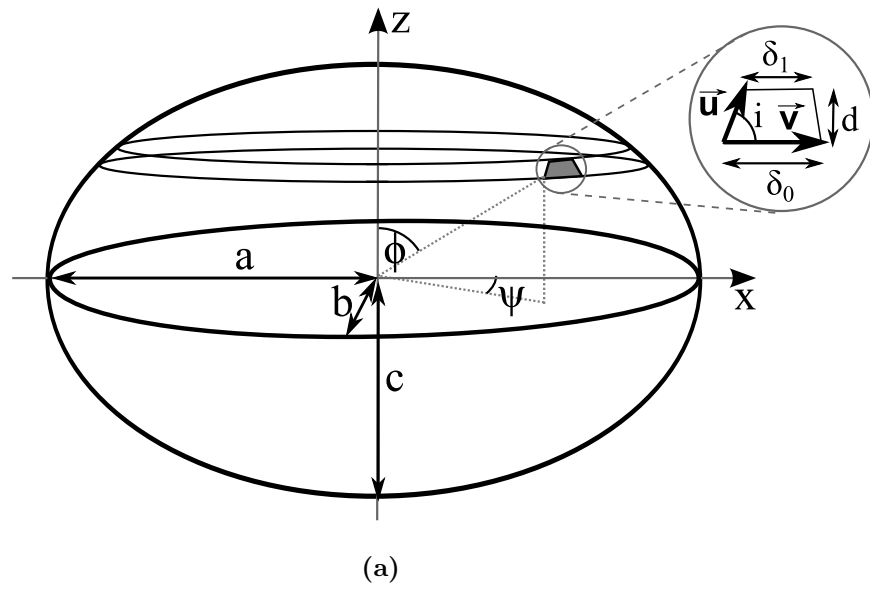
(a)

(b) *Ellipse parallel to (x,y) plane at a height z*

Figure A.3: *Method used to calculate the surface area of an ellipsoidal cap*

the surface area of the rings is not trivial because of how the area element, dA, has to be defined - see FigureA.3. The aim of this calculation is to numerically solve the double integral below

$$S = \int_{\phi=0}^{\theta} \int_{\psi=0}^{2\pi} dA \tag{A.38}$$

to obtain the total surface area, S, of the cap. The first step is to take the ellipse parallel to the (x,y) plane at a height z with radii R_x and R_y defined by equations

$$R_x = a\sqrt{1 - \left(\frac{z^2}{c^2}\right)} \qquad\qquad R_y = b\sqrt{1 - \left(\frac{z^2}{c^2}\right)} \qquad (A.39)$$

It can be shown that the distance between a point $P(x, y, z)$ and the origin $(0, 0, z)$ of the ellipse is given by

$$R(\psi) = \frac{R_x R_y}{\sqrt{(R_x \sin \psi)^2 + (R_y \cos \psi)^2}} \qquad (A.40)$$

where ψ is the angle formed between this length and the x axis. Using this we can define points on this ellipse with the parametric equations

$$x = R \cos \psi \qquad\qquad y = R \sin \psi \qquad (A.41)$$

Now, consider the trapezoidal area element shown in figure A.3. The area of a trapezoid is simply given by

$$dA = \frac{1}{2} \left(\delta_1 - \delta_0\right) d \qquad (A.42)$$

where δ_1 and δ_0 are the lengths of the top and bottom of the trapezoid that are separated by distance d.

In order to calculate d we define two the two vectors, $\mathbf{u}$ and $\mathbf{v}$, along the base and the side of the trapezoid as shown in Figure A.3. The angle between $\mathbf{u}$ and $\mathbf{v}$, ζ is given by

$$\mathbf{u} \cdot \mathbf{v} = |\mathbf{u}||\mathbf{v}| \cos \zeta \tag{A.43}$$

$$\zeta = \arccos \left(\frac{\mathbf{u} \cdot \mathbf{v}}{|\mathbf{u}||\mathbf{v}|} \right) \tag{A.44}$$

The distance d can then be given from the following component of $\mathbf{u}$

$$d = |\mathbf{u}| \sin \zeta \tag{A.45}$$

All of these parameters can be calculated numerically. By splitting each disk of the ellipsoidal cap into a large number of these elements of area dA, the surface area of each disk, dS, can be calculated by summing the elements. The ellipsoid can be split into N disks whose surface area can in turn be summed giving the total surface area of the ellipsoidal cap S. The average height can therefore be given by

$$\bar{h} = \frac{1}{S} \sum_{i=1}^{N} h_i dS_i \tag{A.46}$$

where h_i is the height of the disk evaluated in iteration i from the base of the ellipsoidal cap.

Appendix B

Making Superhydrophobic Surfaces

The approach used to make superhydrophobic surfaces is that of Deng et al. who used the structure of candle soot on a glass microscope slide [19]. The key steps to this process are outlined below.

Glass microscope slides or a silicon wafer were held over the flame of a candle until there was a thick coating of carbon on the surface (the glass was completely opaque). The use of very thin layers, which can be advantageous because they are essentially transparent, was not taken as transparency is not a property we needed and the process seemed more repeatable with thicker layers.

These layers of soot are superhydrophobic because of the morphology of the surface. However, they were incredibly fragile and droplets of water placed on the surface picked up soot which damaged the surface and contaminated the drops. The aim of the rest of the process is to preserve this morphology but make the surfaces more robust.

A simple chemical vapour deposition (CVD) process was used to coat the carbon in silica (carbon dioxide). The carbon coated slides were placed in a desiccator also containing two open beakers containing ~ 2 mL of tetraethoxysilane (TES) and ammonium hydroxide (both from Sigma Aldrich). Over a period of 24 hours, they react forming a carbon/silica network on the surface of the substrates. The samples were then placed in an open tube furnace preheated to 600°C. After two hours, the air had caused combustion of the excess carbon from the sample (only the carbon in the carbon/silica network remains) . The thickness of the original carbon coating determines how opaque this layer is. The furnace was turned off with the samples still inside allowing them to cool slowly stopping the glass substrates from cracking from being cooled quickly. The substrates now have a white colour rather than a black colour.

A final CVD process was then used to reduce the surface energy of the sample. Approximately 1 mL of trichloro(1H,1H,2H,2H-perfluoroocytyl)silane was placed in an open beaker in a desiccator containing the samples. After 12-18 hours, this process was complete. The surfaces now form contact angles of $\sim 150^o$ for a wide rage of liquids including water, oil, toluene and hexadecane.

All chemicals were from Sigma Aldrich. Both CVD processes were done in air at atmospheric pressure and at room temperature.

Bibliography

[1] A. J. James, B. Vukasinovic, M. K. Smith, and A. Glezer, Journal of Fluid Mechanics **476**, 1 (2003).

[2] B. Vukasinovic, M. K. Smith, and A. Glezer, Journal of Fluid Mechanics **587**, 395 (2007).

[3] F. Mugele, J. Baret, and D. Steinhauser, Applied Physics Letters **88**, 204106 (2006).

[4] X. Noblin, A. Buguin, and F. Brochard-Wyart, The European Physical Journal Special Topics **166**, 7 (2009).

[5] S. Mettu and M. K. Chaudhury, Langmuir : the ACS journal of surfaces and colloids **27**, 10327 (2011).

[6] K. R. Langley and J. S. Sharp, Langmuir : the ACS journal of surfaces and colloids **26**, 18349 (2010).

[7] P. Gravesen, J. Branebjerg, and O. S. Jensen, Journal of Micromechanics and Microengineering **3**, 168 (1993).

[8] H. A. Stone, A. D. Stroock, and A. Ajdari, Annual Review of Fluid Mechanics **36**, 381 (2004).

[9] P. Yager *et al.*, Nature **442**, 412 (2006).

[10] J. S. Sharp, D. J. Farmer, and J. Kelly, Langmuir : the ACS journal of surfaces and colloids **27**, 9367 (2011).

[11] F. Hansen, Journal of Colloid and Interface Science **160**, 209 (1993).

[12] J. S. Sharp, Soft Matter **8**, 399 (2011).

[13] R. Hill and L. Eaves, Physical Review E **81**, 1 (2010).

[14] J. Brillo, I. Egry, and T. Matsushita, International Journal of Thermophysics **27**, 1778 (2006).

[15] F. Millot, J. C. Rifflet, G. Wille, V. Sarou-Kanian, and B. Glorieux, Journal of the American Ceramic Society **85**, 187 (2004).

[16] W. Rhim, K. Ohsaka, P. Paradis, and R. Spjut, Review of Scientific Instruments **70**, 2796 (1999).

[17] H. Kusumaatmaja, R. J. Vrancken, C. W. M. Bastiaansen, and J. M. Yeomans, Langmuir : the ACS journal of surfaces and colloids **24**, 7299 (2008).

[18] J. Y. Chung, J. P. Youngblood, and C. M. Stafford, Soft Matter **3**, 1163 (2007).

[19] X. Deng, L. Mammen, H. Butt, and D. Vollmer, Science (New York, N.Y.) **335**, 67 (2012).

[20] S. Daniel and M. K. Chaudhury, p. 3404 (2002).

[21] X. Noblin, R. Kofman, and F. Celestini, Physical Review Letters **102**, 1 (2009).

[22] L. Rayleigh, Proceedings of the Royal Society of London **29**, 71 (1879).

[23] H. Lamb, *Hydrodynamics*, 6th ed. (Cambridge University Press, 1879).

[24] W. Thomson, Philosophical Magazine Series 5 **10**, 109 (1880).

[25] S. Chandrasekhar, Proceedings of the London Mathematical Society **s3-9**, 141 (1959).

[26] I. Egry, G. Lohoefer, and G. Jacobs, Physical Review Letters **75**, 4043 (1995).

[27] I. Egry, G. Lohoefer, I. Seyhan, S. Schneider, and B. Feuerbacher, Applied Physics Letters **73**, 462 (1998).

[28] T. Ishikawa, J. Okada, P. Paradis, and Y. Watanabe, *JAXA Research and Development Report: Improvement of viscosity measurements using oscillation drop techniques with electrostatic levitators.* (Japan Aerospace Exploration Agency, 2010).

[29] C. Vicente, W. Yao, H. Maris, and G. Seidel, Physical Review B **66**, 1 (2002).

[30] E. Beaugnon, D. Fabregue, D. Billy, J. Nappa, and R. Tournier, Physica B: Condensed Matter **294-295**, 715 (2001).

[31] C. L. Shen, W. J. Xie, and B. Wei, Physical Review E **81**, 1 (2010).

[32] R. Hill and L. Eaves, Applied Physics Letters **100**, 114106 (2012).

[33] J. Leiterer *et al.*, Annals of the New York Academy of Sciences **1130**, 78 (2008).

[34] A. L. Yarin, M. Pfaffenlehner, and C. Tropea, Journal of Fluid Mechanics **356**, 65 (1998).

[35] E. Trinh and T. G. Wang, Journal of Fluid Mechanics **122**, 315 (2006).

[36] E. Trinh, A. Zwern, and T. G. Wang, Journal of Fluid Mechanics **115**, 453 (2006).

[37] B. Glorieux and F. Millot, International journal of Thermophysics **20**, 1085 (1999).

[38] F. Millot, J. C. Rifflet, and G. Wille, International journal of Thermophysics **23**, 1185 (2002).

[39] S. K. Chung, D. B. Thiessen, and W. Rhim, Review of Scientific Instruments **67**, 3175 (1996).

[40] T. Richardsen and G. Lohofer, International journal of thermophysics **20**, 1029 (1999).

[41] H. Kobatake, H. Fukuyama, I. Minato, T. Tsukada, and S. Awaji, Applied Physics Letters **90**, 094102 (2007).

[42] R. Hill and L. Eaves, Physical Review Letters **101**, 1 (2008).

[43] R. J. a. Hill *et al.*, Journal of the Royal Society: Interface **9**, 1438 (2012).

[44] M. V. Berry and A. K. Geim, European Journal of Physics **18**, 307 (1997).

[45] C. E. Dijkstra *et al.*, Journal of the Royal Society: Interface **8**, 334 (2011).

[46] M. Strani and F. Sabetta, Journal of Fluid Mechanics **141**, 233 (1984).

[47] M. Strani and F. Sabetta, Journal of Fluid Mechanics **189**, 397 (1988).

[48] F. Celestini and R. Kofman, Physical Review E **73**, 1 (2006).

[49] D. V. Lyubimov, T. P. Lyubimova, and S. V. Shklyaev, Physics of Fluids **18**, 012101 (2006).

[50] X. Noblin, A. Buguin, and F. Brochard-Wyart, The European physical journal. E, Soft matter **14**, 395 (2004).

[51] H. Y. Erbil, Surface free energy and surface tension of liquids, in *Surface Chemistry of Solid and Liquid Interfaces*, chap. 3.2.4, pp. 86–90, Blackwell Publishing, 2006.

[52] J. Berthier and K. Brakke, Droplets: Shape, Surface and Volume, in *The Physics of Microdroplets*, chap. 3, p. 83, Wiley, 2012.

[53] C. Tropea, A. L. Yarin, and J. F. Foss, Surface tension and interfacial tension of liquids, in *Springer Handbook of Experimental Fluid Mechanics*, , Gale virtual reference library No. v. 1, chap. 3.2, pp. 96–106, Springer, 2007.

[54] P. G. de Gennes, F. Brochard-Wyart, and D. Quere, Laplace Pressure, in *Capillarity and Wetting Phenomena: Drops, Bubbles, Pearls, Waves*, chap. 1.1.4, pp. 6–9, Springer, 2003.

[55] R. G. Dean and R. A. Dalrymple, Review of hydrodynamics, in *Water Wave Mechanics for Engineers and Scientists*, Advanced Series on Ocean Engineering, chap. 2.2, pp. 7–19, World Scientific, 1991.

[56] N. B. Vargaftik, B. N. Volkov, and L. D. Voljak, Journal of Physical and Chemical Reference Data **12**, 817 (1983).

[57] P. H. Bigg, British Journal of Applied Physics **18**, 521 (1967).

[58] G. Vazquez, E. Alvarez, and J. M. Navaza, Journal of Chemical & Engineering Data **40**, 611 (1995).

[59] H. Doe and T. Kitagawa, Bulletin of the Chemical Society of Japan **58**, 2975 (1985).

[60] J. G. Webster, Surface Tension Measurment, in *The Measurement, Instrumentation and Sensors Handbook*, chap. 31, Springer, 1999.

[61] P. de Gennes, Reviews of Modern Physics **57**, 827 (1985).

[62] R. Tadmor, Langmuir : the ACS journal of surfaces and colloids **20**, 7659 (2004).

[63] L. D. Landau and E. M. Lifschitz, Surface phenomena, in *Fluid Mechanics*, chap. 7, pp. 238–250, Pergamon Press, , 2nd ed., 1987.

[64] L. D. Landau and E. M. Lifschitz, Damping of gravity waves, in *Fluid Mechanics*, pp. 92–94, Pergamon Press, , 2nd ed., 1987.

[65] S. T. Milner, Journal of Fluid Mechanics **225**, 81 (2006).

[66] D. A. Cummings, D. L.; Blackburn, Journal of Fluid Mechanics **224** (1991).

[67] R. Hill and L. Eaves, Physical Review E **85**, 2011 (2012).

[68] S. Mettu and M. K. Chaudhury, Langmuir : the ACS journal of surfaces and colloids **28**, 14100 (2012).

[69] H. Y. Erbil, Wilhelmy plate method, in *Surface Chemistry of Solid and Liquid Interfaces*, chap. 6.4.2, pp. 238–242, Blackwell Publishing, 2006.

[70] D. M. Henderson and J. W. Miles, Journal of Fluid Mechanics **275**, 285 (2006).

[71] W. M. Haynes, Surface tension of common liquids, in *CRC Handbook of Chemistry and Physics*, CRC Handbook of Chemistry and Physics, pp. 6–182, Taylor & Francis, 2012.

[72] R. C. Weast, M. J. Astle, and W. H. Beyer, *CRC Handbook of Chemistry and Physics*, 6th ed. (CRC Press, 1988).

[73] D. Khismatullin and A. Nadim, Physical Review E **63**, 1 (2001).